Department of Advanced Materials Science
Graduate School of Frontier Sciences
The University of Tokyo

2022

Master's Thesis

Thermal stability of Li-rich cathode under long-duration

(リチウム過剰正極の長時間使用における熱安定性に関する研究)

Submitted July 20, 2022

Advisor: Professor Yoshihisa Harada

趙 昊憧

Haochong Zhao

Table of content

Chapter 1 Introduction

1.1 Lithium-ion Battery

The lithium-ion battery (LiB) is an energy converter which can converts chemical energy into electric energy and vice versa[1,2]. High energy density of LiB has attracted great attention to chemical energy storage[3]. It has undergone great development in the past decades and has been widely used in our daily life, such as in electronic products, since the initial commercialization in the early 1990s. However, the present energy density and thermal stability limit the further application of electric vehicles or electric aircraft[4].

A battery contains a cathode, an anode and electrolyte basically[3]. For LiB it also needs current collector to hold cathode and anode powders and conduct electrons. In case of commercialized lithium cobalt oxide battery, as shown in **Figure 1.1**, when charging de-lithiation and oxidation reaction occurs at cathode side and lithiation and reduction reaction occurs at anode side; During discharging, the reaction goes in reverse. Half reaction at cathode and anode side is shown in Eq (1) and Eq (2).

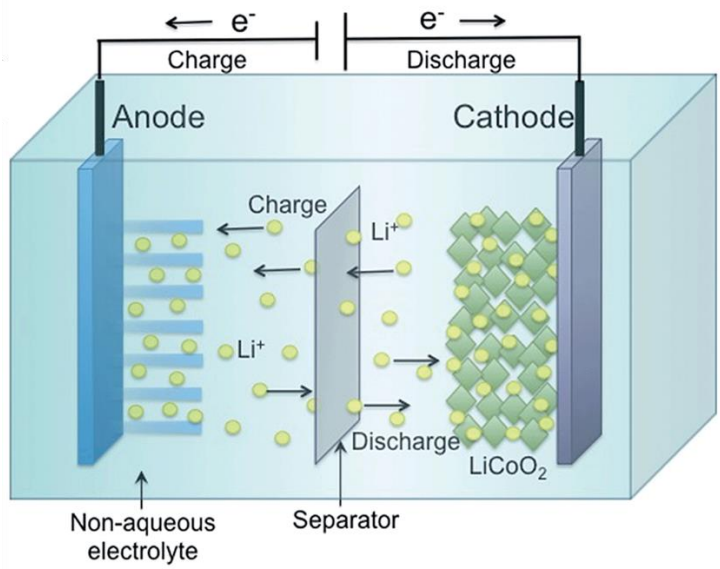

Figure 1.1 Schematic diagram of the lithium intercalation–de-intercalation reaction mechanism in a rechargeable lithium-ion battery[5].

Cathode side:

$$LiCoO_2 \leftrightarrow Li_{1-x}CoO_2 + xLi^+ + xe^- \quad \text{Eq (1)}$$

Anode side:

$$C + xLi^+ + xe^- \leftrightarrow Li_xC_6 \quad \text{Eq (2)}$$

For LiB, there are several properties we need to consider. First is the energy density (Wh/kg). Energy density of a LiB, only considering the cathode and anode materials, the two main performance parameters are electric potential (V, vs Li/Li+) and capacity (mAh/g or Ah/kg). The energy density is shown in Eq(3).

$$\text{Energy density} = \int (E_{cathode} - E_{anode}) \cdot dC \quad \text{Eq (3)}$$

Here, E is electric potential and C is capacity.

The energy density of current lithium-ion batteries is around 100-200 Wh/kg, which is still hard to be an alternative energy source for gasoline[6].

Secondly, the cycling stability of LiB is also an important issue. The structure stability of electrode and reaction on the interface area, cathode-electrolyte and anode-electrolyte interface, is the key point to keep high energy retention during the insertion and de-insertion of Li-ion[7-10].

Figure 1.2 Evident damage in the battery after runaway.[11]

Besides, the thermal stability of Li-ion battery is also an important issue to limit the further application. The layered cathodes with high energy density usually have lower degradation temperature and cause thermal runaway[12-16]. Such problems seriously threaten the safety of users, as shown in **Figure 1.2**.

In conclusion, aiming for further application, the development of cathode and anode materials with higher energy density, higher cycling and thermal stability are the main targets.

1.2 Composition of Li-ion battery

1.2.1 Anode materials

There are 3 main anode materials, graphite, silicon, and metallic lithium, respectively. Graphite is the commercialized anode materials since 1990s with capacity of 372 mAh/g and 0.1-0.2V (vs. Li^+/Li) [17,18]. **Figure 1.3** shows the schematic of Li insertion in graphite. It has the advantages of good cycle performance, low cost and small volume expansion.

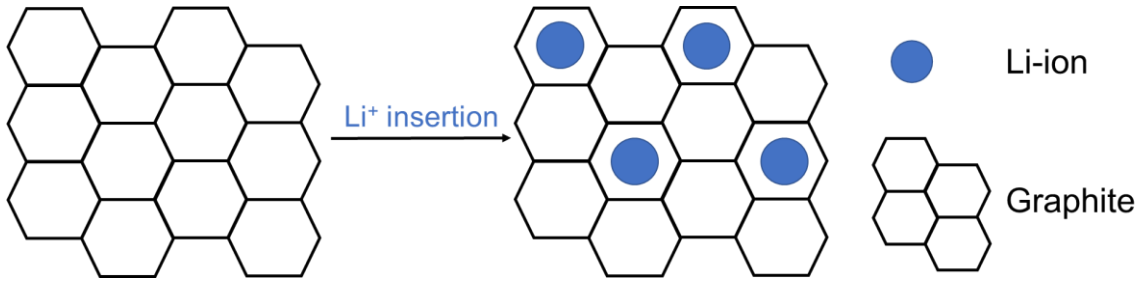

Figure 1.3 Schematic of Li insertion into graphite.

Silicon-based anode materials show much higher capacity of 4200mAh/g with low electric potential of ~0.06V (vs. Li^+/Li)[17]. However, due to large volume expansion (400% volume change) in during charge/discharge process[19,20], it is now used as a nano anode additive with graphite.

Li metal or alloy anode shows the highest capacity since it does not need any other skeleton structure. Whereas the inhomogeneous deposition and dissolution

of dendrite lead to failure on application of Li metal anode. The dendrite Li metal easily puncture the separator leading to short circuits, and it usually appears inactive, resulting in a loss of battery capacity[21,22]. As a result, Li metal anode now is only in laboratory experiment.

1.2.2 Electrolyte

As a medium for conducting lithium ions, the electrolyte is an important part of LiB. The electrolyte requires high Li-ion conductivity(>10^{-3}S/cm), low electronic conductivity and good electrochemical stability at cathode-electrolyte and anode-electrolyte interface[3,23-26].

Usually, the electrochemical stability at interface can be described by HOMO-LUMO theory. As shown in **Figure 1.4**, a ideally stable electrolyte should have large electrochemical window. In that case, the HOMO of electrolyte is lower than LUMO of cathode so that the electron will not migrate from electrolyte to cathode and cause the oxidation of electrolyte. Similarly, the LUMO of electrolyte should also be higher than HOMO of anode to prevent reduction. However, there is less electrolyte can have so large electrochemical window. Usually, commercialized electrolytes do not have enough electrochemical window but it will have some reaction at interface to stabilize the electrolyte. The formation at interface is called cathode-electrolyte interface (CEI) and solid electrolyte interface (SEI) which can be stable with cathode and anode thermodynamically or kinetically.

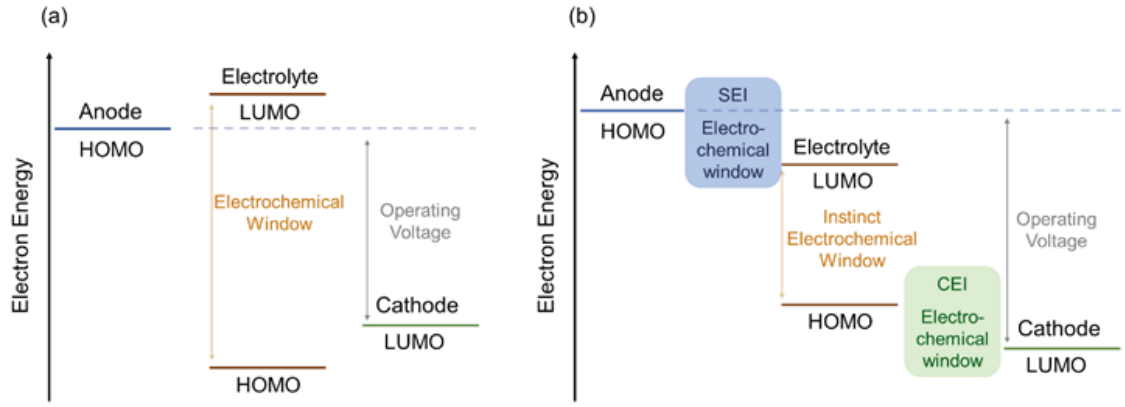

Figure 1.4 The electrochemical stability of electrolyte. (a) Ideal electrolyte (b) Practical electrolyte

For nonaqueous liquid electrolytes, a commercialized electrolyte in LiB, ethylene carbonate (EC), dimethyl carbonate (DMC), diethyl carbonate (DEC), and ethylmethyl carbonate (EMC) are the main component with ~5×10^{-3}S/cm at ambient temperature[23]. Such liquid electrolytes, after the first cycle, is electrochemically stable with at the interface due to the formation of CEI and SEI[3]. However, liquid electrolytes is organic and flammable under high temperature. It is easy to catch fire with a small short circuit or poor cooling system.

Another kind of potential electrolyte is solid-state electrolyte (SSB). There are two main kinds of SSB, oxide and sulfide. Both have good thermal stability than liquid electrolyte.

Oxide solid-state electrolytes usually are not toxic in ambient atmosphere and are more stable with cathode electrochemically. Though recent researches show that they do not have a large electrochemical window as previously thought, fortunately oxide electrolyte will also form a stable CEI at cathode interface and is kinetically stable[8,9,24,27-32]. However, the high hardness of oxides generally results in poor interfacial contact and thus lead to a low overall ionic conductivity[3,25]. As a result, the oxide solid electrolytes are often combined with tiny amount of liquid electrolyte to improve interface contact.

Sulfide solid-state electrolytes have higher Li-ion conductivity, even higher than that of liquid electrolytes (~10^{-2}S/cm)[26]. Also, they are usually softer and have good contact with cathode and anode. However, sulfide electrolytes do not have large electrochemical window and the electrochemical potential of Li-ion is much higher than that in cathode. Thus Li-ion tends to migrate from electrolyte to cathode side and form a “space charge layer” with low Li-ion conductivity.

As a result, though solid state is inflammable and have good thermal safety, they still face problems on application. Moreover, the burning of the electrolyte is only part of the thermal runaway and cannot be completely solved even with solid electrolytes.

1.2.3 Cathode materials

1.2.3.1 Spinel type

$LiMn_2O_4$ is a typical spinel phase cathode material proposed by Thackeray et al[33]. The O^{2-} lattice structure is closely related to α-$NaFeO_2$ but the cation is not in the same order. As shown in **Figure 1.5 (a)**, the transition metal (TM) is available at octahedral site and Li-ion is located at tetrahedral site.

The half reaction of $LiMn_2O_4$ is shown in Eq (4):

$$LiMn_2O_4 \leftrightarrow Mn_2O_4 + Li^+ + e^- \qquad \text{Eq (4)}$$

This reaction is an obvious phase transition reaction and have a voltage plateau around 4V[34]. The maximum theoretical capacity is 148mAh/g but usually it can only reach 100-120mAh/g in practical[35]. The problems with this cathode material are Jahn-Teller effect of Mn^{3+} and the disproportionation and dissolution of Mn^{2+}[35,36]. The electronic structure of Mn^{3+} and Jahn-Teller effect is shown in **Figure 1.6.**

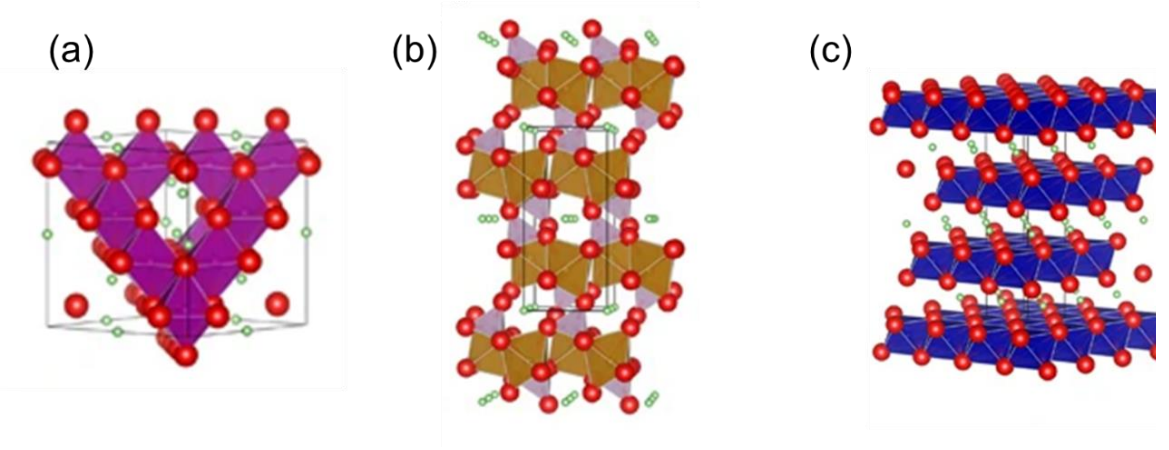

Figure 1.5 Crystal structure of (a) spinel $LiMn_2O_4$, (b) olivine $LiFePO_4$, (c) layered $LiCoO_2$[37].

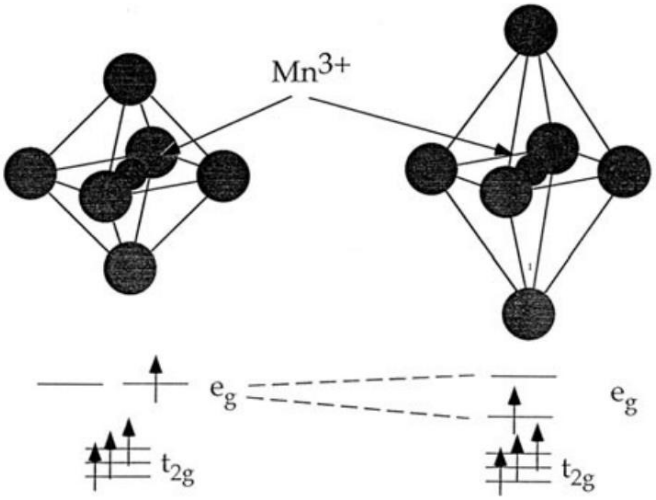

Figure 1.6 The Jahn–Teller distortion of an octahedron around Mn^{3+} splits the degenerate e_g levels[36].

1.2.3.2 Olivine type

$LiFePO_4$ is a typical kind of olivine type cathode material found by the group of Goodenough in 1997[38]. The structure of olivine $LiFePO_4$ is shown in **Figure 1.5(b)** It has many advantages as follows:

(1) Cheap and low toxicity Fe is used.

(2) It shows proper electric potential (3.4 V vs. Li + / Li) as redox of Fe^{3+}/ Fe^{2+}.

(3) High structural stability and thermal stability.

(4) Theoretical capacity is 170 mAh/g. Energy density is 550 Wh/kg, and it is close to conventional oxide-based cathode materials ($LiNi_{0.5}Co_{0.2}Mn_{0.3}O_2$: ~650 Wh/kg).

However, with the development of layered cathode materials, lack of energy density begins to be a problem because $LiFePO_4$ is close to its theoretical energy density.

Another attractive olivine cathode material is $LiMnPO_4$. The biggest merit of $LiMnPO_4$ is its higher redox potential (4.1V vs. Li^+/Li) than $LiFePO_4$ which can bring 20% additional energy density. Whereas $LiMnPO_4$ has received less

attention than his $LiFePO_4$ because its electrical conductivity is much lower (about 3-5 orders of magnitude) than his $LiFePO_4$.[39]

1.2.3.3 Layered type

Nowadays, the layered cathode materials have been widely used. J.B Goodenough first found α-$NaFeO_2$ type cathode materials, $LiCoO_2$ (LCO) in 1980[40]. The crystal structure is shown in **Figure 1.5 (c)**. Co^{3+} is located at octahedral center of O^{2-}. The stacking order of O is O3-type (ABCABC). LCO can provide 0.5-0.6 Li-ion per unit with 4.2-4.35V cut-off voltage (142-160mAh/g)[41-44].

After LCO, researcher found other TM can also form such layered structure, such as $LiNi_{0.33}Co_{0.33}Mn_{0.34}O_2$. All these layered cathode materials are arranged in this order: O layer, TM layer, O layer, Li layer. So, this layered structure can also be written as $LiMO_2$ (M=Ni, Co, Mn). In this paper, we call it "normal layered cathode".

In 1990s, Li_2MnO_3, which was once thought to be an electrochemically inactive material, showed good reversible capacity around 4.5V[45,46]. Li_2MnO_3 have excess Li-ion on TM layer in order and it can also be written as $Li_{4/3}Mn_{2/3}O_2$ as shown in **Figure 1.7(b)**. Here, the valence state of Mn is +4 and it is inactive. The electrochemical activity is originated from redox of O. Thus, the oxygen redox and anion redox has gained tremendous attraction in recent years in LiB or sodium ion battery.

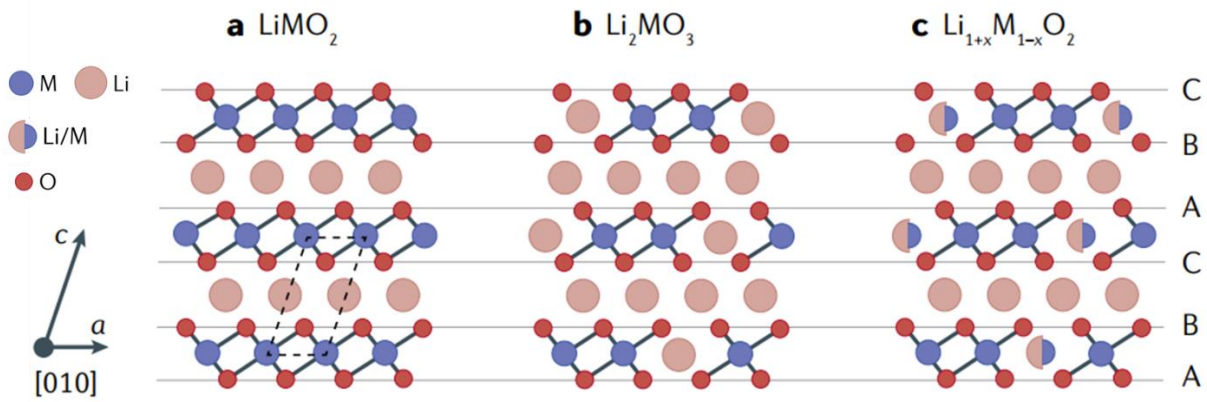

Figure 1.7 Lattice structure of (a) $LiMO_2$, (b) Li_2MO_3 and (c) Li-rich cathode[47].

The Li-rich cathode materials is related to normal layered cathode and Li_2MnO_3. The lattice structure is shown in **Figure 1.7(c)**. In 1997, Koichi Numata et al. found solid solution $LiCoO_2$-Li_2MnO_3 but unfortunately, they did not charge it over 4.5V and miss the excess capacity of this material[48,49]. Lu et al. first found the excess capacity of Li-rich cathode over 4.5V. It is a solid solution of $LiMO_2$-Li_2MnO_3(M=Ni, Co, Mn) and shows capacity over 300mAh/g. Though the capacity is much higher than normal layered cathode, it also has unique problems: the severe hysteresis in 1st cycles and voltage fading during cycling, as shown in **Figure 1.8**.

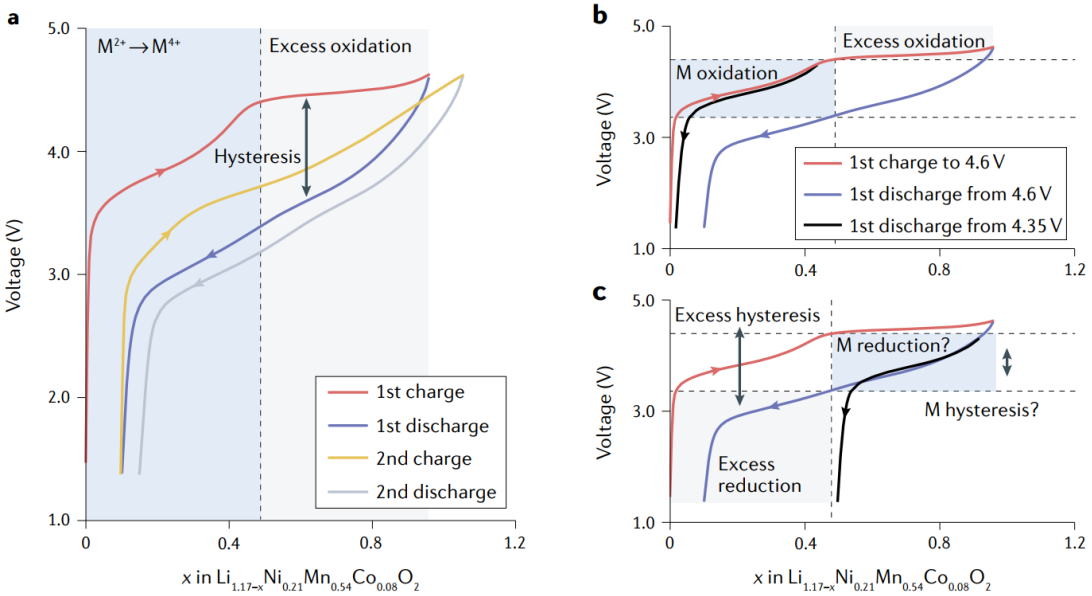

Figure 1.8 Voltage curves for Li-rich cathodes. (a) Illustration of the common features, including the activation plateau at ~4.5V and persistent hysteresis. (b) The voltage curve changes upon discharge only after being charged through the activation plateau above 4.5 V. (c) One potential discharge mechanism wherein the order of conventional and anion redox switch. The discharge curve of the partially charged electrode (black) is shifted so that it overlies the discharge curve of the fully charged electrode (blue) at the beginning of discharge.[47]

The origin of hysteresis in 1st cycle and voltage fade is related to O_2 release due to the instability of oxidized O^{n-} at surface area[7,50,51] and the TM migration[52-54]. The former can be improved by surface coating but the latter is much harder to solve because it is an intrinsic property of the cathode material under high de-lithiation.

The lattice structure and electronic structure difference between normal layered and Li-rich cathode materials, will cause interesting difference on redox mechanism and electrochemical performance, which will be shown in the next section.

1.3 Comparison between normal layered and Li-rich cathode materials

1.3.1 Electrochemical performance

Before introducing the electronic structure and TM migration, the electrochemical performance difference is shown first. This is consistent with the research process of researcher at that time.

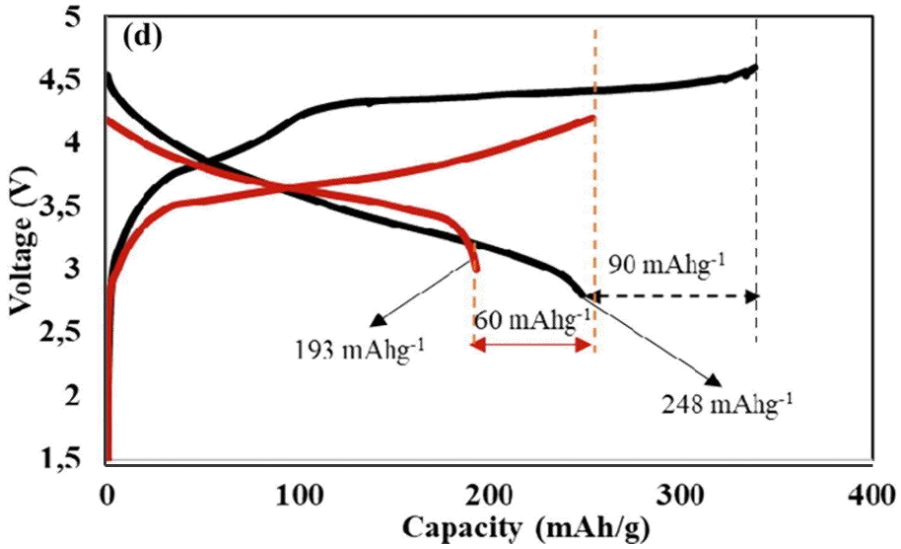

Figure 1.9 Charge–discharge profiles of $LiMn_{0.33}Co_{0.33}Ni_{0.33}O_2$ (red line) and $Li_{1.252}Mn_{0.557}Ni_{0.123}Co_{0.126}Al_{0.0142}O_2$ (black line).[55]

Figure 1.9 is a typical comparison between of $LiMn_{0.33}Co_{0.33}Ni_{0.33}O_2$ (red line) and Li-rich cathode materials. There are two obvious "plateaus" during 1st charge process and more capacity than normal layered cathode. However, the charge and discharge curves of Li-rich cathode is not symmetric, which cause

typical hysteresis in 1st cycles. During the cycling, there is also a severe voltage fade as shown in **Figure 1.10**. In contrast there is almost no voltage fade in normal layered cathode.

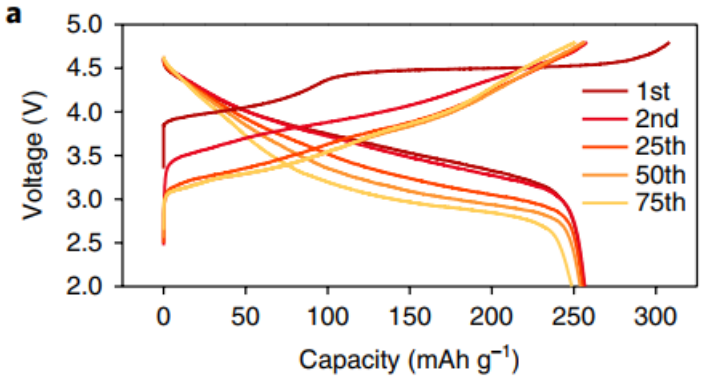

Figure 1.10. Charge–discharge curves for $Li_{1.2}Ni_{0.15}Co_{0.1}Mn_{0.55}O_2$ for the 1st, 2nd, 25th, 50th and 75th cycles.[7]

The excess capacity is from the independent oxidation of O^{2-} to O^{n-}. The excess Li-ion and redox species bring more capacity in Li-rich cathode than normal layered cathode.

1.3.2 Electronic structure and Transition metal migration

1.3.2.1 Electronic structure

In previous section, the difference on lattice structure and electrochemical performance is shown in **Figure 1.7** and **Figure 1.9** respectively. The electronic structure is highly related to the coordination environment and the Li-ion in TM layer will cause an interesting coordination change and it will lead a change on redox mechanism and electrochemical performance. Considering Li-rich cathode and Li_2MnO_3 have similar lattice structure (Li-ion in TM layer) and electrochemical properties (redox plateau around 4.5V), the electronic structure also have the similarities.

As shown in **Figure 1.11**, in normal layered cathode materials, every O are coordinated with 3 Li-ion and 3 transition metal. In this case, all O 2p orbitals have hybridization with TM 3d, 4s or 4p orbitals. There is no localized O 2p orbitals. The orbitals close to Fermi level usually is t_{2g} and e_g*, which is dominated by TM but not O. As a result, in normal layered cathode materials, it is mainly

TM provide and accept electron during cycling. More recently, some researchers found the O 2p-TM 3d hybridization and ligand to metal charge transfer (LMCT) is nonnegligible. As a result, O also attributes to redox with TM-O hybridization. For example, in $LiCoO_2$, Co t_{2g} is not fully localized and has hybridization with O 2p[41,56,57].

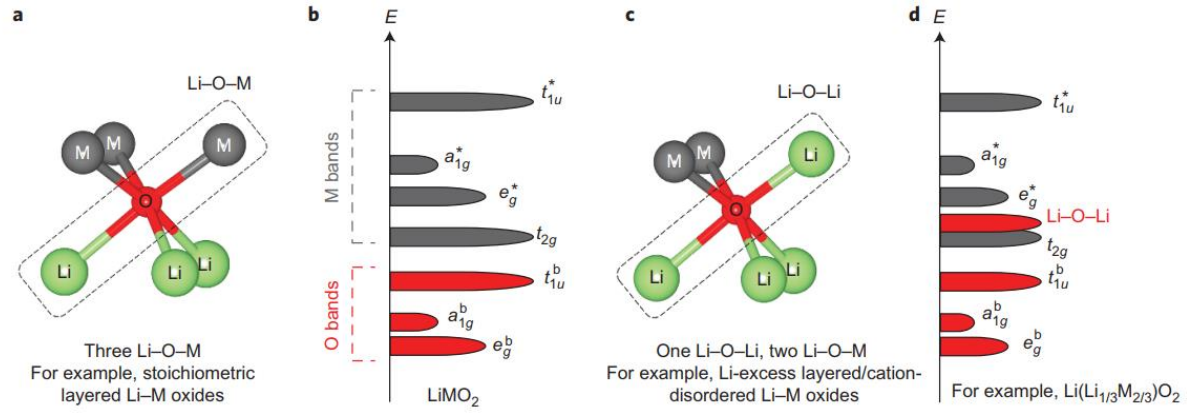

Figure 1.10 (a) Local coordination around O in normal layered cathode. (b) Schematic of the electronic structure for normal layered cathode such as $LiCoO_2$. (c) Local coordination around O with one Li–O–Li a in Li-rich layered or Li_2MnO_3. (d) Schematic of the electronic structure for Li-rich layered cathode such as Li_2MnO_3.[58]

In contrast, in Li-rich and Li_2MnO_3 materials, due to the excess Li-ion in TM layer, some O is coordinated with 4 Li-ion and 2 TM as shown in Figure 1.10(c). There will be a localized and nonhybridized O 2p orbital along this "Li-O-Li" axis because Li-ion is fully ionized with O. Note that O 2p orbital is higher than most TM t_{2g} orbitals and Ni^{4+} Co^{4+} and Mn^{4+} has no electron on e_g* orbitals, the energy of localized O 2p orbital closer to Fermi level and provide electron during charge and discharge[58,59]. More recently, some researchers pointed out that the localized O 2p will have π interaction with TM 3d orbitals to stabilize the oxidized O species in a way[60,61].

Figure 1.11(a) shows the localized O 2p orbitals on the top of valence band in Li_2MnO_3 and **Figure 1.11(b)** shows the charge transfer from O 2p to Co t_{2g} (red circle) in $LiCoO_2$ with resonant inelastic X-ray scattering (RIXS) measurement.

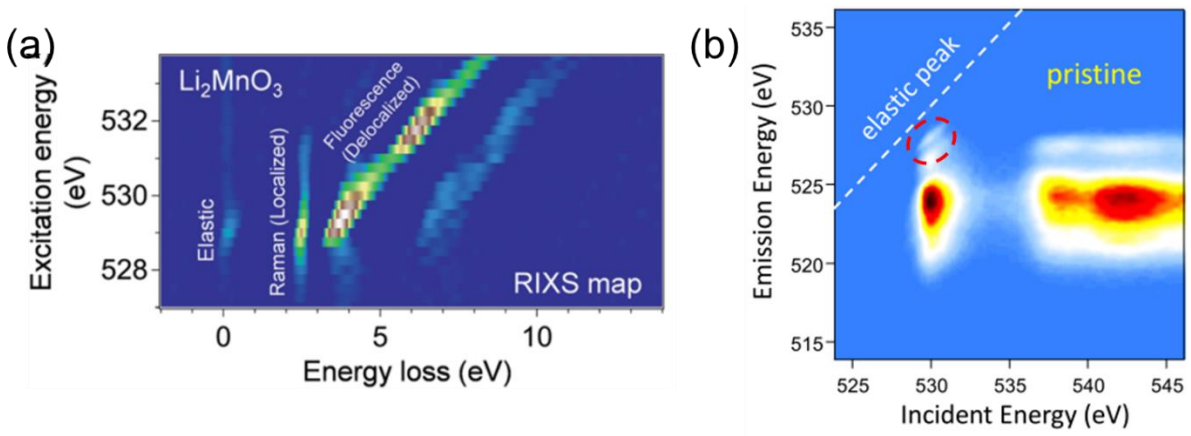

Figure 1.11. (a) RIXS map of Li_2MnO_3, the Raman-like peak refer to localized O 2p orbital. (b) RIXS map of $LiCoO_2$, the weak peak in red circle refer to charge transfer from O to Co.

1.3.2.2 Transition metal migration

In Li-rich cathode, the higher amount of de-lithiation bring more Li vacancies and thus cause TM migration more easily to occur. As shown in **Figure 1.12**, after 1st cycle, there is a severe disorder of cation in Li-rich cathode.[53]

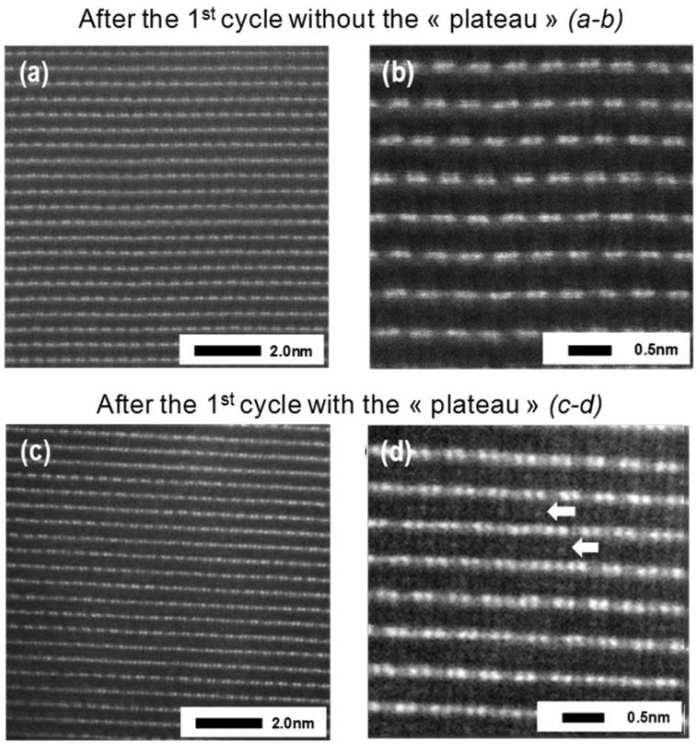

Figure 1.12. HAADF-STEM images of the material recovered after the first cycle (a and b) without the 4.5V "plateau". (c and d) with the 4.5V "plateau" (2-4.8V).

The migration of TM may have huge influence on hysteresis on 1st cycle because some "Ribbon-ordered" structure (TM hard to migrate) material with similar anion redox shows almost no hysteresis during cycling. However, due to limitation of present characterization methods, the TM migration cannot be observed clearly and people can only get the average information but not single layer information. As a result, whether the migration of transition metals is randomly disordered or segregated is still under arguing[54,62-68].

1.3.3 Redox mechanism

For normal layered cathode, the redox mechanism is simpler. As mentioned in previous introduction, the orbital near Fermi level in $LiMO_2$(M=Ni, Co, Mn, with valence state of +3) is t_{2g} or e_g* orbitals. According to ligand field theory and molecular orbital theory, TM t_{2g} has less π interaction with O 2p. e_g* is the result of severe σ interaction between TM e_g and O 2p orbitals but the energy level of TM e_g is higher than O 2p orbitals so the e_g* is also dominated by TM e_g orbital, As shown in **Figure 1.13(a)**. In conclusion, both of these orbitals are dominated by TM with some hybridization with O.

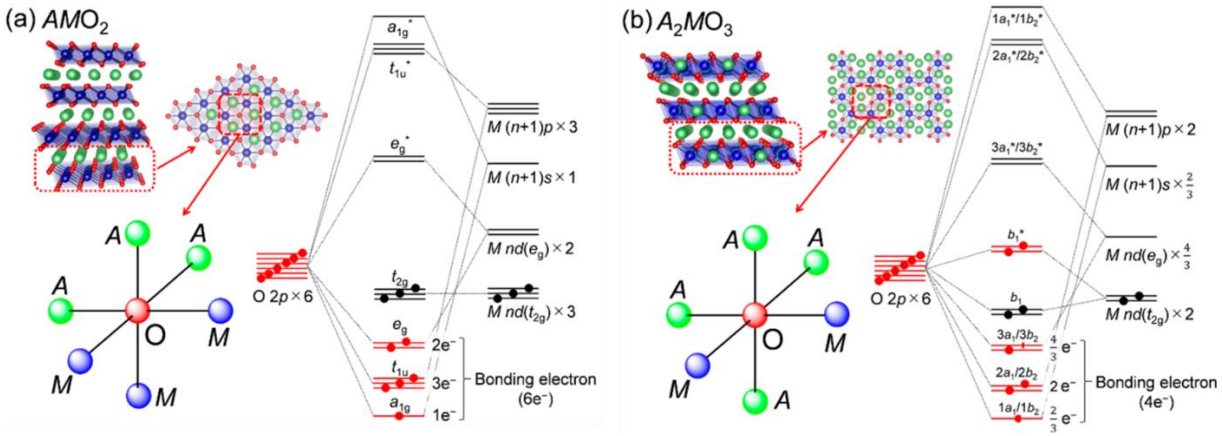

Figure 1.13 Molecular orbital energy diagrams of (a) AMO_2 and (b) A_2MO_3.The electronic structure of M is assumed as for t_{2g}^6 e_g^0 simplicity.

The Li-rich cathode is solid solution of $LiMO_2$-Li_2MnO_3. The $LiMO_2$ component will bring the similar redox mechanism as normal layered cathode materials which is related to the first "plateau" in charge and discharge curves. For Li_2MnO_3 component, the electronic structure is shown in **Figure 1.13(b)**. The

second “plateau” around 4.5V is related to the redox of O and the electron is provided by localized O 2p orbitals with only tiny hybridization with t_{2g} orbital.

However, though the origin of excess capacity is the localized O 2p orbital, the detailed mechanism of redox is still under arguing. Some researchers think the O^{2-} is oxidized to O_2^{n-} which is called O-O dimmer, like peroxide bonding[69,70]. However, there is also researchers using neutron diffraction to indicate that the shortened distance between interlayer O is far away to form a σ bonding, like peroxide[71]. More recently, with the help of high resolution RIXS and neutron diffraction measurement, the formation and participation of O_2 molecule have been reported[62-64]. Meanwhile, some researcher thought the weak π interaction between TM t_{2g} and O 2p will be strengthened at charged state because of the decrease in atomic distance but it needs lithium sites do not aggregate.

Either hypothesis need to put the effect of TM and Li-ion migration in consideration. As a result, the detailed redox mechanism needs multiple scales of characterization of lattice structure and electronic structure.

Although the detailed mechanism is still a mystery, the utilization of abundant oxygen redox and formation of a high valence state of oxygen (O^{n-}, $0 \leq n < 2$) is a certain characteristic of Li-rich cathode materials. The formation of high valence state oxygen at charged state may have influence on the thermal behavior because it may not be stable.

1.4 Thermal behavior of layered cathode materials

1.4.1 Thermal behavior and degradation of layered cathode materials

With the increase on energy density of LiB, more and more thermal runaway accident with layered cathode has been reported. For a commercialized LiB, the thermal degradation is a complicated process. Generally, short circuit or charging heat leads to degradation of electrolyte and anode and at this stage, it releases heat slowly. But when the temperature is high enough to cause the phase transition of cathode side, the de-lithiated layered cathode will release abundant heat very fast

and cause fire[12]. As a result, the thermal behavior of layered cathode is a key point to determine the thermal safety of a LiB.

The thermal behavior of normal layered cathode and Li-rich cathode has similarities. Both of them will have layered → spinel → rock salt phase transition, and the spinel phase transition is the most important thermal release reaction in LiB[13,15,16]. The in-situ heating XRD result is shown in **Figure 1.14**. The orange lines indicate the start of the spinel phase transition.

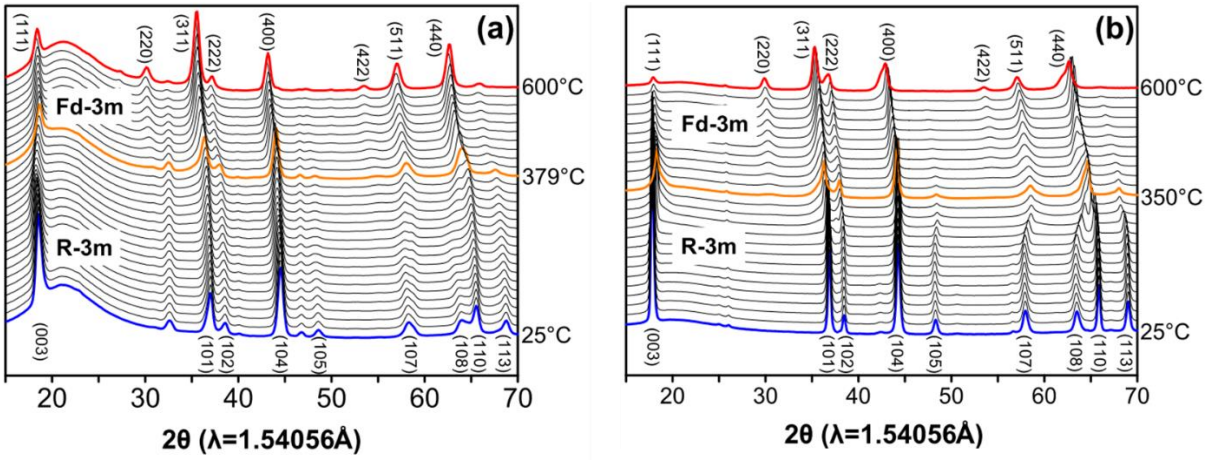

Figure 1.14 In situ X-ray diffraction results of charged (a) $0.5LiMn_{0.33}Co_{0.33}Ni_{0.33}O_2$-$0.5Li_2MnO_3$ and (b) $LiMn_{0.33}Co_{0.33}Ni_{0.33}O_2$ cathode during heating from 25 to 600℃ without electrolyte.

Previous study focused on the thermal behavior on first two cycles. However, there is a complicated change on lattice and electronic structure during the 1st cycles and it also reflected on the electrochemical performance. For a practical LiB, the first several cycles are carried out in factory and user uses batteries after the first cycle. As a result, it is also important to investigate the thermal behavior change under long-duration.

1.4.2 Differential scanning calorimetry (DSC) measurement

DSC is a technique in which the difference in energy input into a substance and a reference material is measured as a function of temperature, while the substance and reference material are subjected to a controlled temperature program. In short, DSC measures the heat flow during the reaction or phase transition.

This measurement is a very commonly used method to study the thermal properties of cathode materials. **Figure 1.15** shows the DSC results of Li-rich cathode material in first and second cycles. The first peak around 300℃ is related to spinel phase transition reaction and it is the main reason for heat runaway. At around 450℃, the second peak is usually related to the degradation of PVDF binder and carbon powder in cathode samples which is necessary for a coin cell.

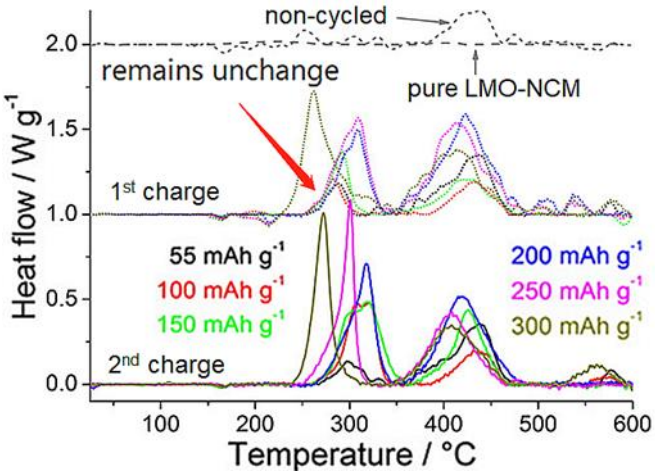

Figure 1.15. DSC curves of Li-rich cathode at different state of charge in the first (dotted line) and second (solid line)[15]

In this research, I am focusing on the heat flow of the spinel phase transition with long cycled Li-rich cathode materials which is related to first peak intensity.

1.5 Electrochemical characterization of cathode materials

Much research has focused on the electronic state of cathode materials for LiBs. As specific experimental methods, X-ray photoelectron spectroscopy (XPS) and X-ray absorption spectroscopy (XAS) are often used to elucidate the electronic structure occupied state and unoccupied state[72-75]. Especially, resonant X-ray photoemission spectroscopy (RXPS) is a powerful method to investigate the valence band structure. However, due to the strong correlation interaction of between TM and O, the electronic structure of the valence band and

conduction band (band near Fermi level), which is directly involved in the charge / discharge reaction, is a complex mixture of oxygen and transition metals. So, it still faces difficulty in distinguishing the characteristic and attribution of each band. More recently, non-resonant X-ray emission spectroscopy (XES) and resonant inelastic X-ray scattering (RIXS) has been utilized to investigate the spin state evolution[76,77] and high valence state oxygen[60,63,64,78-81]. The schematic of XAS, XES, XPS and RIXS is shown in **Figure 1.16**.

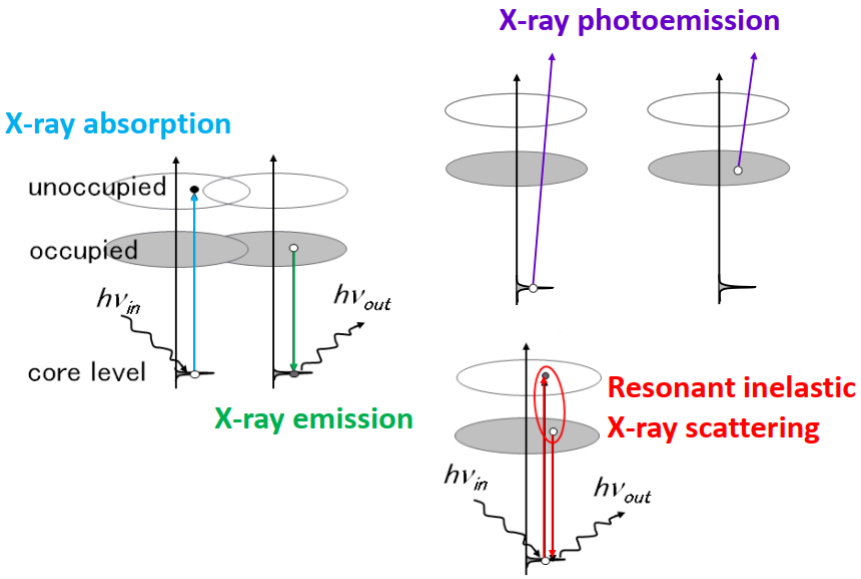

Figure 1.16. Schematic of XAS, XES, XPS and RIXS

It is worth noting that, as mentioned in previous section, in transition metal oxide, the TM 3d with hybridization of O 2p is usually near the Fermi level. As a result, we need to consider energy level splitting of 3d orbitals, charge transfer (CT) and Mott-Hubbard theory while analyzing the experimental and theoretical results.

1.6 Purpose of this research

There are many factors and properties that can influence the application of LiBs and one of them is the thermal safety. There are some researches focusing

on the thermal behavior in Li-rich cathode at the 1st and 2nd cycle. However, at long-duration (long cycles), which user may face, there is lack of research of thermal behavior, especially in a deeper electronic and lattice structure aspect.

In order to elucidate the thermal behavior mechanism in thermodynamic and kinetic, in this paper, I performed XAS, XPS and (resonant X-ray photoelectron spectroscopy) RXPS to characterize the electronic structure evolution under long duration. From the electronic structure, the lattice structure information will also be visualized. Combining with electronic structure and lattice structure, I hope to elucidate the mechanism of thermal behavior.

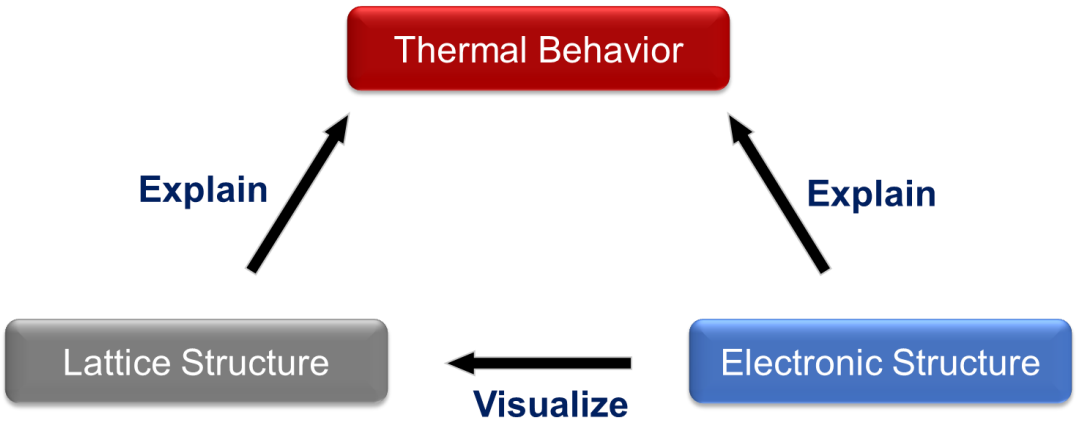

Figure 1.17. The method to utilize electronic structure characterization to explain the thermal behavior of Li-rich cathode.

Chapter 2 Methods and Experiments

2.1 Sample preparation and electrochemical characterization

The Li-rich cathode materials, $Li_{1.2}Mn_{0.54}Ni_{0.13}Co_{0.13}O_2$ compounds, were prepared by co-precipitation method from Institute of Physics Chinese Academy of Sciences.

The positive electrode was made of the active material mixed with 10% of carbon black and 10% of polyvinylidene fluoride (PVDF) in N-methyl pyrrolidinone (NMP) solvent. The blended slurries were pasted onto an aluminum foil, followed by cutting to 12 mm in diameter and drying at 120℃ in vacuum for 10 h. The test cell consisted of positive electrode and Li metal as negative electrode separated by a porous polypropylene film and commercialized electrolyte for high voltage (Shanshan Co.) The charge and discharge tests were carried out using a Land CT2001A battery test system (Wuhan, China) in a voltage range of 2.0–4.8 V. The current density was 25 mA/g for the first cycle and 125mA/g for subsequent cycles. At the final cycle, the cell was charged to 4.8V with current density of 25 mA/g. All the cycling was performed at room temperature.

The charge / discharge reaction of cathode is:

$$Li_{1.2}Mn_{0.54}Ni_{0.13}Co_{0.13}O_2 \leftrightarrow Li_{1.2-x}Mn_{0.54}Ni_{0.13}Co_{0.13}O_2 + xLi^+ + e^-$$

After cycling, the charged state coin cells were disassembled immediately. The cathode samples were washed in DMC, dried in vacuum for one night and kept in glove box full of Ar gas.

2.2 DSC measurement

2.2.1 Basic principle of DSC measurement

The heat flow q can be expressed as:

$$q/m = -c_p\beta + \dot{H} \qquad \text{Eq (5)}$$

Here, C_p is the specific heat of the sample, m is the mass of the sample, β is the heating rate and $\dot{H}$ is the heat flow caused by enthalpy change[82]. If the reaction is exothermic, the heat flow $\dot{H}$ is positive. **Figure 2.1** shows the basic structure of differential scanning calorimeter.

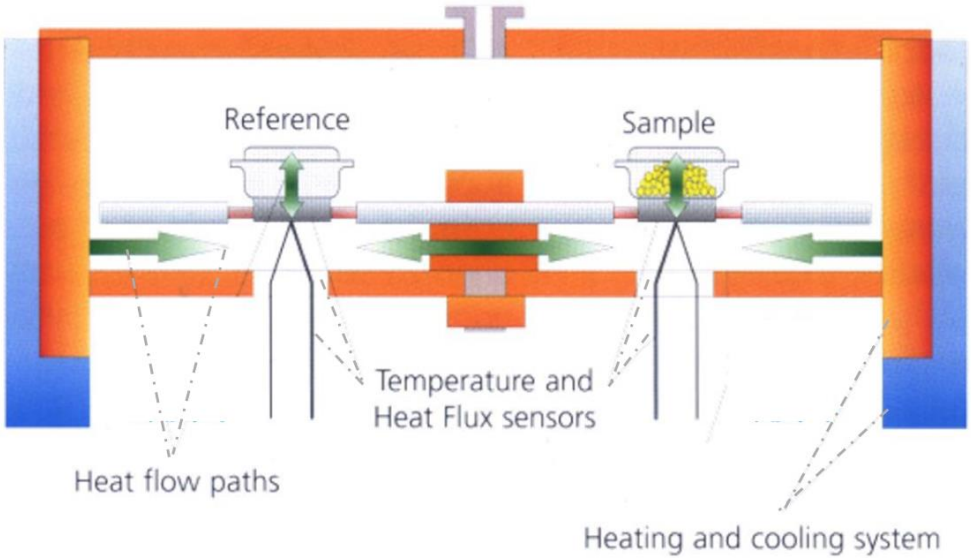

Figure 2.1 Structure of differential scanning calorimeter.

The sample crucible contains the sample and is placed on the sensor plate together with the reference crucible (usually an empty crucible). The sensor is installed in a uniform furnace body, tested according to a certain temperature program (linear heating, cooling, constant temperature or combination). Two pairs of thermocouples (reference thermocouple, sample thermocouple) are used to continuously measure the difference between the temperature difference signal and its change with time t and temperature T.

2.2.2 Experiment method

The washed and dried cathode materials with different cycles (2^{nd}, 50^{th} and 200^{th} at 4.8V) were scratched off from the Al current collector and put into crucible (avoid exposure to air) with Ar gas flow respectively. The DSC measurement was performed between 25°C and 600°C at a scan rate of 10K min^{-1} under a flow of Ar gas.

2.3 X-ray spectroscopy measurement

2.3.1 X-ray absorption spectroscopy (XAS)

XAS is a measurement that utilizes X-ray to excite electrons into an unoccupied state as a function of photon energy. The O K-edge XAS spectrum represents the unoccupied state density of O 2p and TM L-edge spectrum represents the unoccupied state density of TM 3d band. Since TM valence orbitals are hybridized with the O 2p orbitals, O K-edge XAS can also reflect the information of TM 3d, such as coordination symmetry and covalency, at pre-edge peaks. For 3d TM compounds, the L-edge, 2p-3d XAS spectrum, reflects 3d states such as valence state, spin state, and crystal field splitting.

In this study, O *K*-edge, Mn, Co, and Ni *L*-edges XAS were measured by the surface-sensitive total-electron-yield (TEY) mode and the bulk-sensitive partial-fluorescence yield (PFY) mode at HORNET station of SPring-8 BL07LSU. The probing depths of TEY and PFY are less than 10 nm and about 100 nm, respectively.

2.3.2 X-ray photoelectron spectroscopy (XPS)

When a material is irradiated with high-energy X-ray, the electron is emitted and this phenomenon is called “Photoelectric effect”. XPS is an experimental method for measuring the energy distribution of photoelectron and obtaining the

core and valence electron information. The binding energy satisfies the following equation:

$$E_k = h\nu_{in} - E_b - \phi \qquad \text{Eq (6)}$$

Here, E_k is the kinetic energy of emission photoelectron, $h\nu_{in}$ is the excitation energy, E_b is binding energy of selected orbital and ϕ is the work function of samples.

In this study, O 1s, Mn 2p, and valence band were collected on 3DnanoESCA station of SPring-8 BL07LSU. Because of the high binding energy and low concentration of Ni and Co, it is hard to get the good high-quality signal of core level. The excitation energy is 1000eV for every measurement.

2.3.3 Resonant X-ray photoelectron spectroscopy (RXPS)

When the excitation energy is matched with the absorption energy from the core level to the valence band, the resonant photoelectron emission occurs, as shown in **Figure 2.2**. When the resonant excitation occurs, there are 2 processes. First is the direct photoemission (set TM as an example):

$$p^6d^N + h\nu_{in} \longrightarrow p^6d^{N-1} + e^- \qquad \text{Eq (7)}$$

This process equals to non-resonant XPS of valence band.

The other process is:

$$p^6d^N + h\nu_{in} \longrightarrow p^6d^{N+1} + core\ hole \rightarrow p^6d^{N-1} + e^- \qquad \text{Eq (8)}$$

According to Fano resonance theory, quantum chemical interference occurs[83], resulting in a significant increase on photoemission cross section of 3d electrons of selected element.

In this study, the excitation energy was chosen according to the absorption peaks in XAS results obtained by TEY mode. It is worth noticing that the high valence state O is not obvious in XAS result. As a result, for RXPS in O valence band, I additionally chose an excitation energy of 531eV as the excitation of the high valence state O. Charged cathode samples with 2nd, 50th and 200th cycled were measured.

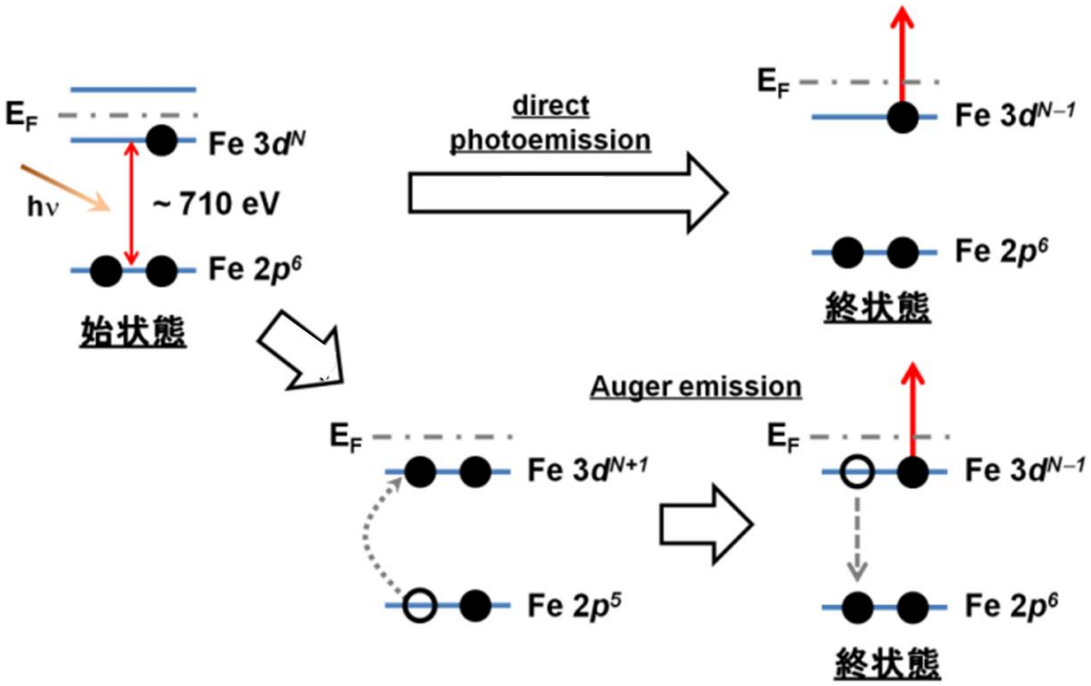

Figure 2.2. Principle of RXPS. Set Fe as an example. [84]

Chapter 3 Electrochemical and DSC Experiments Results and Discussion

3.1 Electrochemical results

Figure 3.1 shows the charge (solid) and discharge (dash-dot) profile of Li-rich cathode material under 200 cycles. The result shows a typical characteristic of Li-rich cathode: At 1st charge process, it has "2 plateaux", which is related to the oxidation of TM and O, respectively. In subsequent charge and discharge, the "plateau" feature disappears and there is no obvious oxidation stage, which means the TM and O redox is mixed at both the charge and discharge process. Also, it is worth noticing that there is a continuous voltage fading, as shown in **Figure 3.2**, due to O_2 release and TM migration.

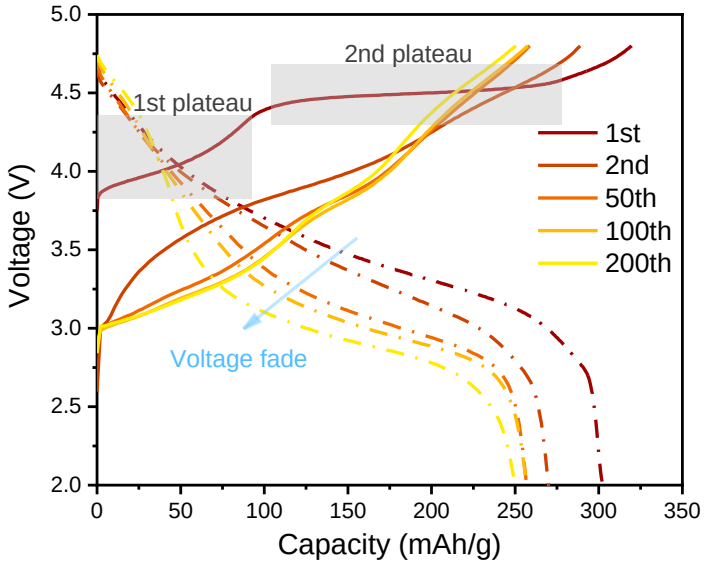

Figure 3.1. Charge(solid)-discharge (dash-dot) curves for Li-rich battery cell with 1st, 2nd, 50th and 100th and 200th cycled.

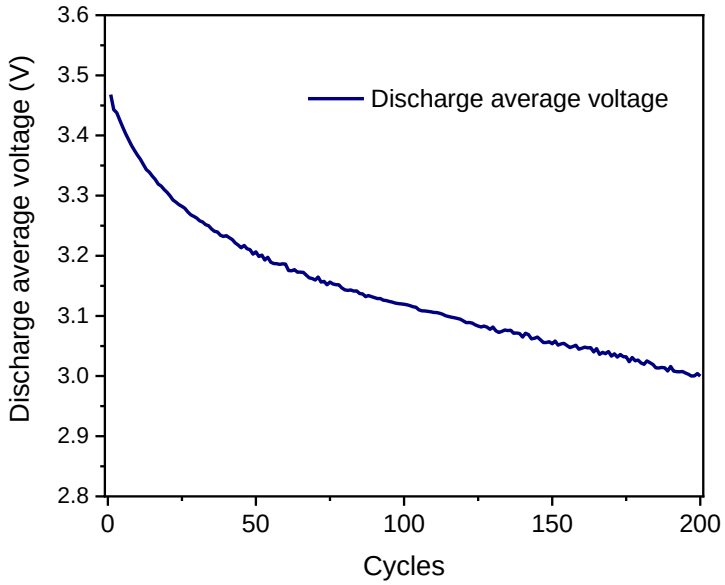

Figure 3.2 Discharge average voltage and voltage fading during cycling.

3.2 DSC results

Figure 3.3 (a) and (b) show the DSC profiles of the charged Li-rich cathode samples with 2nd, 50th and 200th cycles. In order to verify the reproducibility and exclude the possibility of a short circuit during de-assembling of the coin cell, the results of repeated experiments are shown in **Figure 3.3** (b).

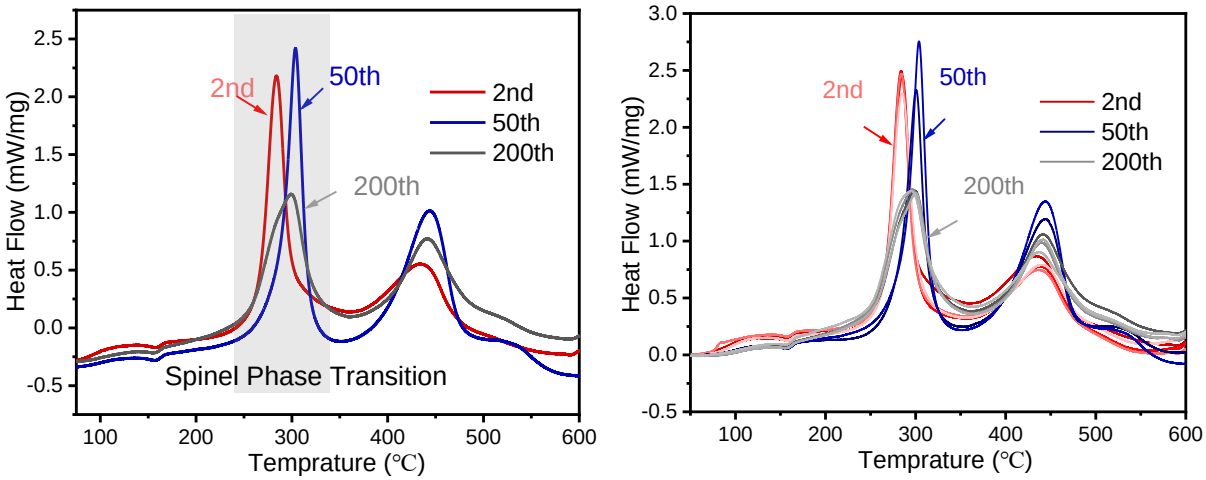

Figure 3.3 DSC curves of (a) 4.8V charged $Li_{1.2}Ni_{0.13}Co_{0.13}Mn_{0.54}O_2$ at the 2nd, 50th and 200th cycles and (b) repeated experiment results.

At the same cycles, all the results show similar features: samples at the 2nd cycles have the lowest onset temperature (~260℃) and at the 50th cycles, the onset temperature has a tiny increase (~275℃), which means the thermal stability has a tiny increase in thermodynamic. However, at the 200th cycles, the phase transition (degradation) onset temperature drops back and is similar to the 2nd samples.

From the heat flow intensity and shape, it is obvious that at the 200 cycles, the phase transition rate becomes slow, which means the reaction is inhibited in kinetic. Whereas there is less change between the 2nd and 50th cycles. The weakening of the reaction kinetics is most pronounced in the 200 cycled sample.

3.3 Discussion and summary

In conclusion, the electrochemical characterization shows typical charge and discharge features and voltage fading, which indicate the sample is a qualified Li-rich cathode material. The disappearance of the redox "plateaus" and voltage fading originated from O_2 release due to oxygen redox and TM migration.

The thermal behavior evolution under long-duration: the phase transition onset temperature first increases and at around the 200th cycles drop back; the phase transition rate first shows less change but a huge drop at the 200th cycled samples. All these features indicate the kinetics and thermodynamics of the reaction have changed obviously under long duration.

Chapter 4 Electronic Structure Characterization Result and Discussion

4.1 XAS results

In order to investigate the mechanism of thermal behavior in Li-rich cathode materials, the charged cathode samples of the corresponding number of cycles are performed for the XAS measurement.

4.1.1 TEY mode results

TEY mode is a surface sensitive measurement and its probing depth is less than 10nm. The XAS results for Ni, Co, Mn *L*-edge obtained by TEY mode are shown in **Figure 4.1.** The poor signal-to-noise ratio of Ni and Co is due to their small content. Ni *L*-edge shows an obvious evolution under long duration: the peak intensity at 855eV shows a huge decrease. The weakening of the peak at 855eV indicates that the reduction of Ni, from +3/+4 to +2[85,86]. Mn also shows a similar reduction from Mn *L*-edge. The appearance of peak shoulder at 640.5eV and 641.9eV indicate the Mn^{+2} and Mn^{+3}, respectively[76,77]. Besides, the absolute intensity of Mn *L*-edge has a decrease under long-duration and it is due to the Mn-Ni segregation, and the concentration of Mn will decrease at the surface area. **Figure 4.1 (d)** shows the visualized spectra of Mn *L*-edge. Both intensities of the Mn^{2+} and Mn^{3+} peaks have increased. The first Mn^{4+} peak at 641eV does not change because it overlaps with the shoulder of Mn^{2+} and Mn^{3+} and the intensity of the second Mn^{4+} peak at 643.5eV have decreased which indicates that Mn has reduction from +4 to +2/+3. However, there is less change on Co *L*-edge because Co^{+3} and Co^{+4} have similar peaks in layered cathode materials, such as $LiCoO_2$ and the only tiny difference is a shoulder peak at 778eV. The reason why Co^{+3} and Co^{+4} are not sensitive at *L*-edge may be related to a substantial charge transfer from O to Co. Though it is hard to see the valence state variation from **Figure 4.1 (b)**, previous research reported that Co would also have some reduction from hard X-ray absorption results[7]. It is no surprise that the TM will

have a reduction during cycling because the O_2 release cannot be 100% inhibited if we utilize the oxygen redox[87-89].

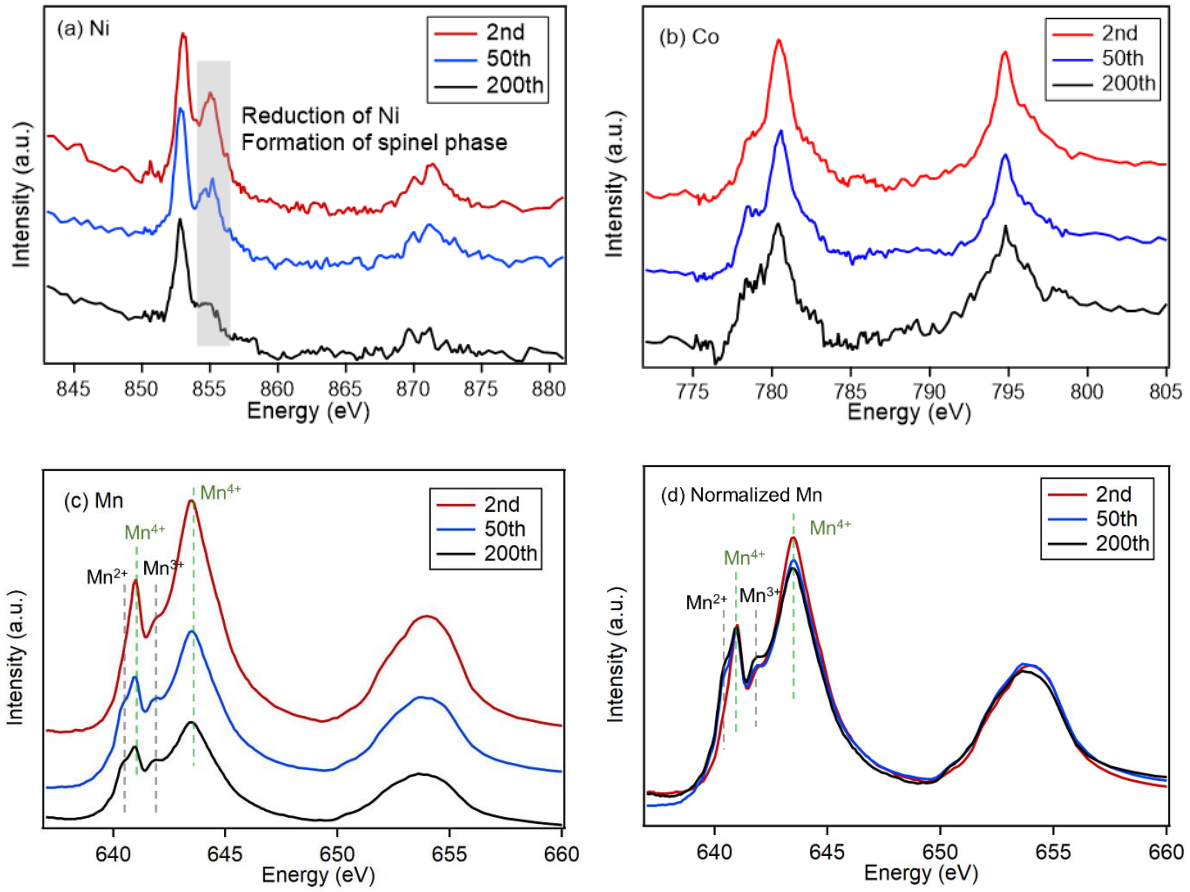

Figure 4.1 (a)Ni, (b)Co, (c)Mn and (d)normalized Mn *L*-edge XAS results obtained by TEY mode

Compared with the electronic evolution of TM, the electronic structure of O is also important because O can be involved in redox in the way of TM-O and localized O 2p redox. **Figure 4.2** shows the O K-edge XAS results obtained from TEY mode. At the pre-edge area, there is an obvious intensity decrease of the peak at 529.5eV and increase of the peak at 531.8eV. Also, the increase of the peak intensity at 537eV and the decrease of the peak intensity at 542.5eV occurs during the cycling. All these features are corresponding to the formation of the spinel phase thin layer at the surface area[50,90,91].

Combined with Ni, Co, Mn *L*-edge XAS results at the surface area, the Ni reduction is not only because of the O_2 release in Li-rich materials but also related to the formation of $LiNi_{0.5}Mn_{1.5}O_4$ (LNMO) type spinel phase. In LNMO the valence state of Ni is around +2 and the oxidation potential is over 4.7V (vs Li^+/Li).

Besides another kind of spinel cathode $LiCoMnO_4$ shows an even higher oxidation potential around 5V (vs Li^+/Li)[92]. Hence, it can explain why the surface area shows electrochemical inactivity and Ni keeps +2 valence state under 4.8V. At last, those electronic structure evolution occurs during the whole cycling process and at the 200th cycles, there are almost no layered structure signals. As a result, combined with previous research[7,50], it indicates that the phase transition from layered to spinel is going to a deep area from the surface during cycling.

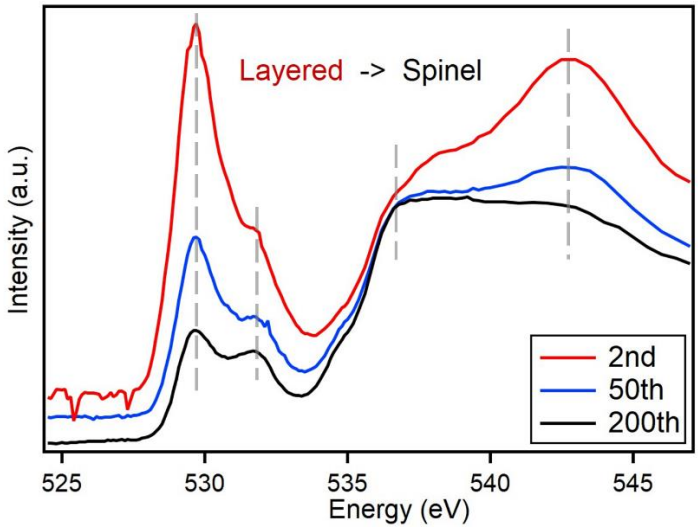

Figure 4.2 O *K*-edge XAS results obtained by TEY mode.

4.1.2 PFY mode results

PFY mode is a bulk-sensitive(~100nm) measurement that collects the emission photon from selected elements. In transition metal oxide, usually there are self-absorption and saturation effects that can distort the line shape of the L_3-edge TFY XAS results. Fortunately, the inverse partial-fluorescence-yield (iPFY) mode can reduce the distortion in spectral line shapes better than the PFY mode. Because the distortion is significant when the O Kα emission is strongly dependent on the excitation energies[76], Cr and Mn usually are suitable for the iPFY mode. Hence, in fluorescence-yield, I extract PFY mode results for all Ni, Co, Mn and O and iPFY mode results for Mn.

The XAS results for TM obtained by PFY and iPFY mode is shown in **Figure 4.3**, which clearly shows that Ni shows reduction in bulk area but the degree of

reduction is weaker than the surface and it is consistent with the fact that oxygen loss is mainly concentrated at the surface. It is also hard to distinguish the valence state variation from **Figure 4.3 (b)** because there is less difference between Co^{3+} and Co^{4+} from XAS results. The PFY and iPFY results of Mn is shown in Figure**4.3 (c) and (d)**. It is obvious that there is difference on peak ratio and shape between PFY and iPFY mode. But both show a very tiny peak at around 641.9eV which indicate the formation of Mn^{3+} and reduction of Mn under long-duration.

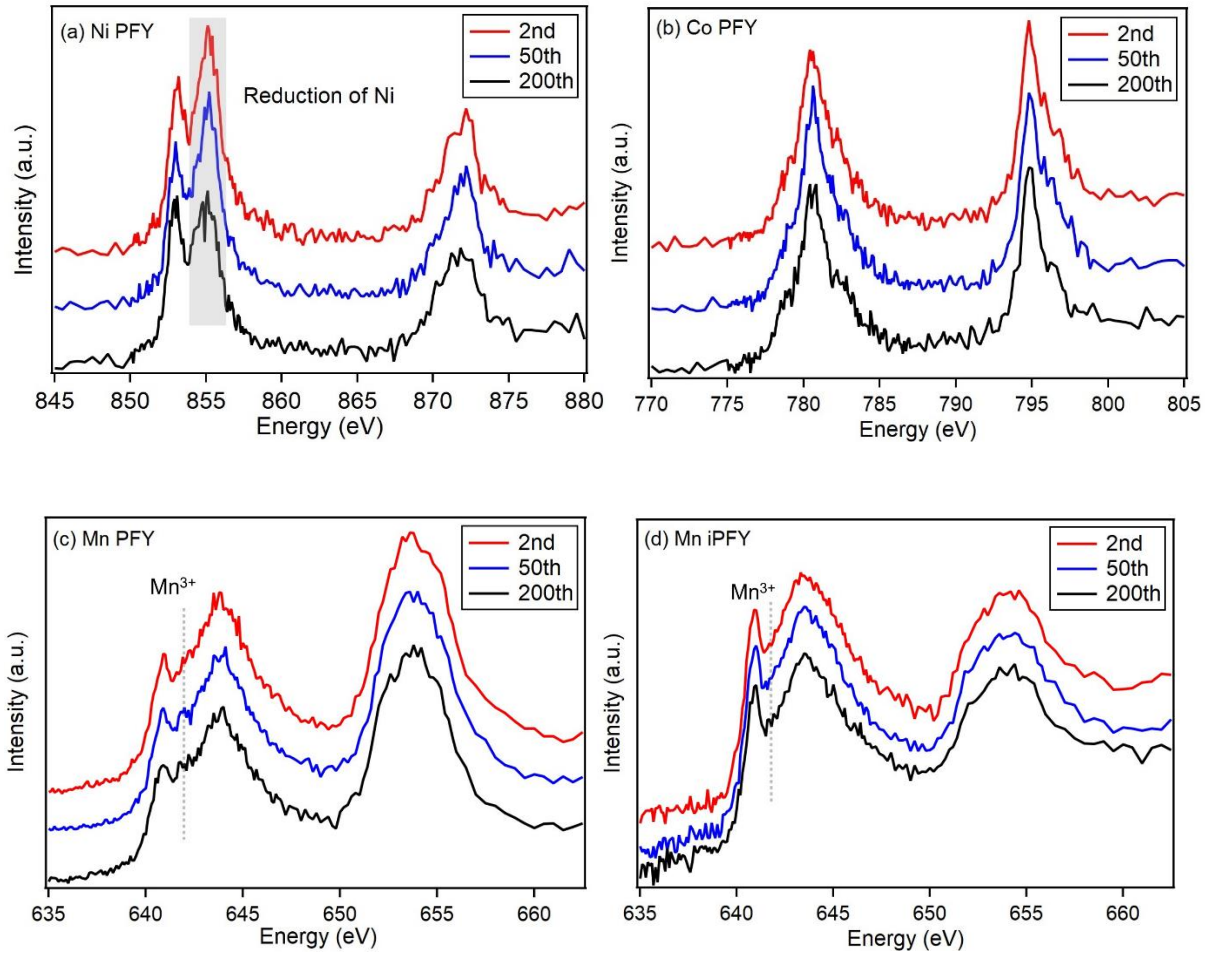

Figure 4.3 (a)Ni, (b)Co, (c)Mn *L*-edge XAS results obtained by TEY mode

The O K-edge XAS results obtained by PFY mode is shown in **Figure 4.4**. In O K-edge XAS, the pre-edge peaks (from 528 to 533 eV) arise from exciting an oxygen 1s electron to unoccupied states that feature hybridization between oxygen 2p and TM 3d states[41,93,94]. The decrease of intensity at the pre-edge area is usually related to the weakening of hybridization between O 2p and TM 3d orbitals. This weakening of hybridization is consistence with the reduction of

TM during cycling. The line shape does not have obvious change, which corresponds to the fact that the layered structure is kept at the bulk area under long-duration.

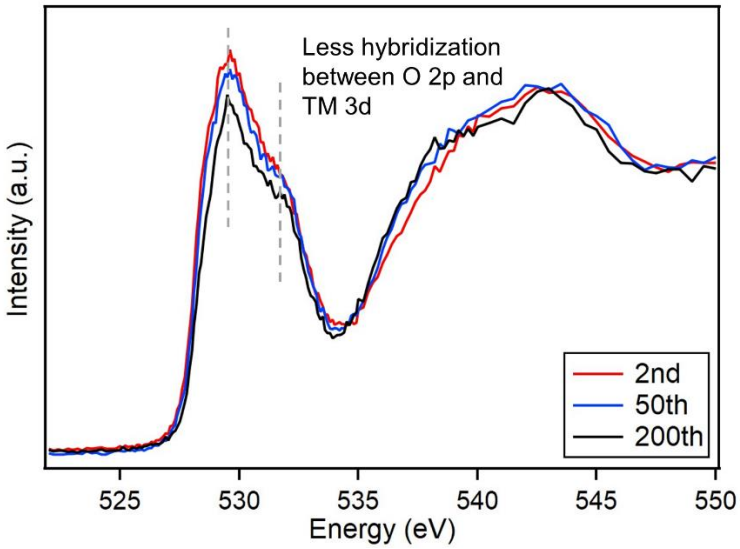

Figure 4.4 O *K*-edge XAS results obtained by PFY mode.

4.1.3 Discussion and summary on XAS results

At the surface area, the XAS results shows a severe reduction of TM and phase transition from layered to spinel. The composition of the spinel phase is LiM_2O_4 or M_3O_4 and the ratio of TM to O is 1:2 or 3:4. Compared with the pristine composition $Li_{1.2}Ni_{0.13}Co_{0.13}Mn_{0.54}O_2$ (the TM: O ratio is 2:5), there is a severe O_2 release. Because the main thermal degradation process is from layered to spinel with O_2 release, the spinel phase formed at surface area is more stable than layered phase during heating. During the heating process, the phase transition and O_2 release start at the surface area first and even the bulk O also needs to diffuse to the particle surface to be released. The stable spinel phase at surface area will inhibit the phase transition and O_2 release kinetically and previous paper also shows that artificial coating of spinel helps improve thermal stability[13]. Accordingly, the thermal degradation rate slowing down can be explained by the formation of the spinel phase at surface area.

In bulk area, the reduction of TM can explain why the onset temperature will have an increase from the 2^{nd} cycles to the 50^{th} cycles[95]. However, though TM

have reduction during cycling continuously, from the 50th cycles to the 200th cycles, the degradation onset temperature drops back in contrast. This indicate that there are some other factors that influencing the onset temperature. TM ions is continuously reduced due to the continuous O_2 release. Some papers report that there may be O defects accumulated in bulk area because of O_2 release. As a results, on the one hand, the O_2 release during cycling will reduce the TM and increase the onset temperature, on the other hand, it will produce oxygen defects, resulting in a decrease in the stability of the lattice structure and a decrease in the temperature. The schematic is shown in **Figure 4.5**.

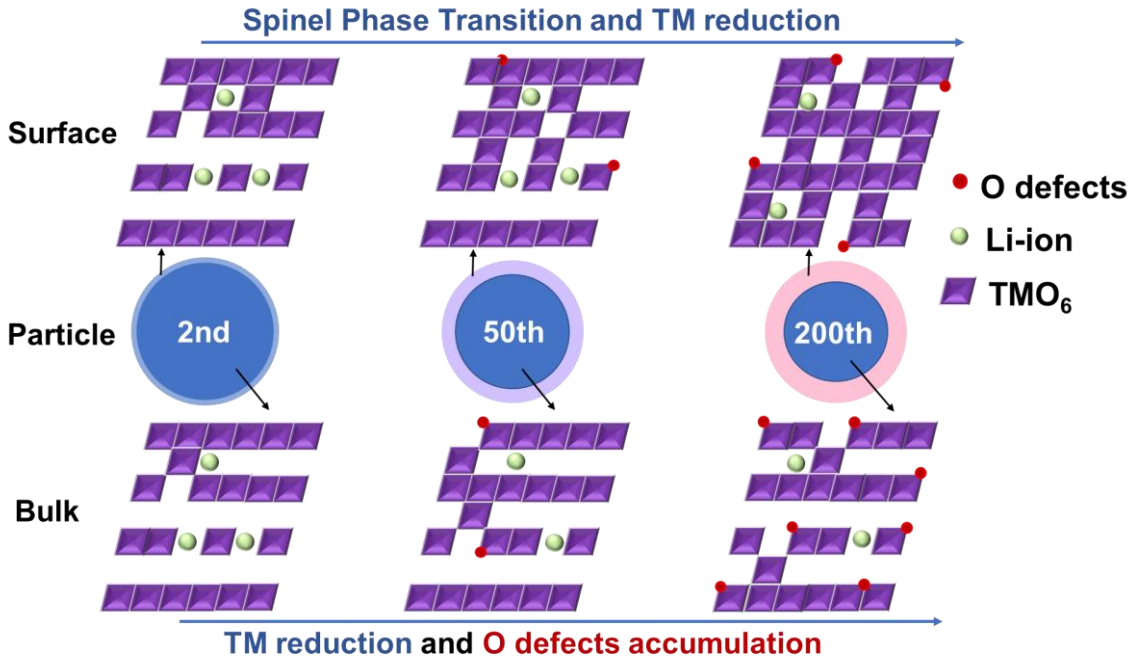

Figure 4.5. Schematic of structure evolution in surface and bulk area under long-duration. Blue words indicate that this factor increases thermal stability, red words indicate that this factor do harm to thermal stability.

4.2 XPS and RXPS results

4.2.1 Core level XPS results

As mentioned in the previous chapter, the electronic structure of Mn 2p and O 1s core level was characterized. From **Figure 4.6(a)**, there is less change on Mn 2p spectroscopy. Previous surface-sensitive TEY mode results show that the amount of reduction of Mn is less than that of Ni, so it can explain why Mn 2p does not have a severe variation.

However, from O 1s XPS results, as shown in **Figure 4.6(b)**, there is a tremendous evolution. Considering the probe depth of XPS and RXPS is 2-3 nm, even less than that of XAS TEY mode, the peak evolution is mainly attributed to the CEI at the cathode particle surface. CEI is a solid mixture formed from the complicated reaction between organic liquid electrolyte and cathode surface during charging and discharging. As a result, O 1s results not only reveal the information from transition metal oxide but also from the organic compounds. The peak with binding energy around 529 eV refers to the transition metal oxide. The peak intensity decreasing at 529 eV indicates that the CEI becomes thicker at the very surface area and transition metal oxide is buried during long-duration.

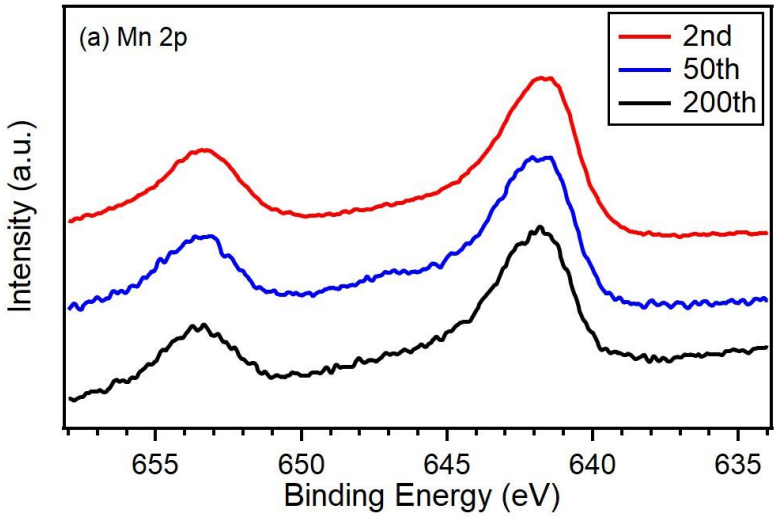

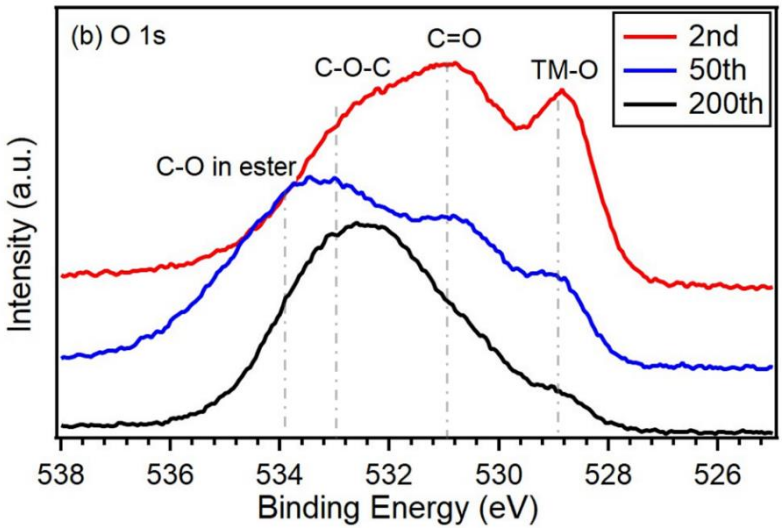

Figure 4.6. XPS results of (a) Mn 2p and (b) O 1s.

The detailed analysis of O 1s spectroscopy is shown in **Figure 4.7**. It is clear to see that the composition of CEI also has a severe change under long-duration. The amount of "C=O" is decreased and "C-O-C" is increased under long-duration. However, it is worth noticing that the peak fit in XPS has much subjective influence, so the specific species of organic compounds may not be very precise to verify. But we can still identify that the CEI has an obvious evolution under long-duration from the line shape.

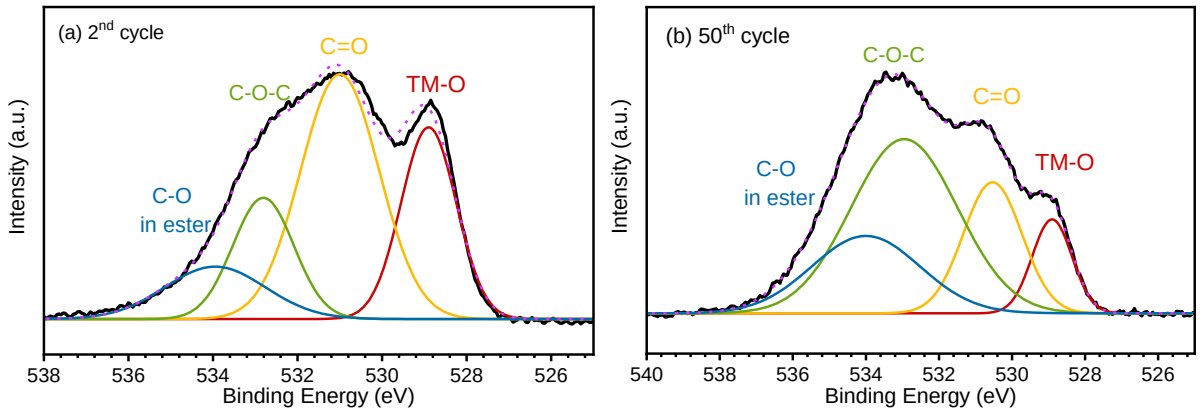

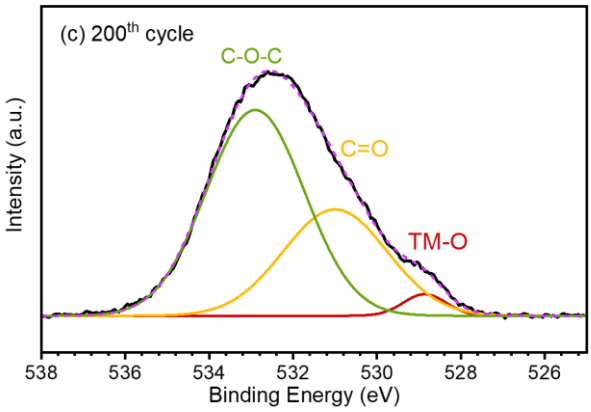

Figure 4.7. Peak fitting of O 1s XPS results with different cycled samples

4.2.2 Valence band and RXPS results

In order to visualize the electronic structure on valence band, the XPS measurement and RXPS measurement on the valence band are performed. **Figure 4.8** shows the valence band structures obtained by XPS measurement and I choose the peak with a binding energy of 9 eV as a normalized peak to see the relative intensity variation near the Fermi level (0 eV). It is obvious to see that near the Fermi level, the intensity shows a decrease which indicates that the electrons transfer to a deeper energy level. The result shows fewer electrons at the Fermi level and it can explain the electrochemical inactivity at the surface area from XAS TEY mode results.

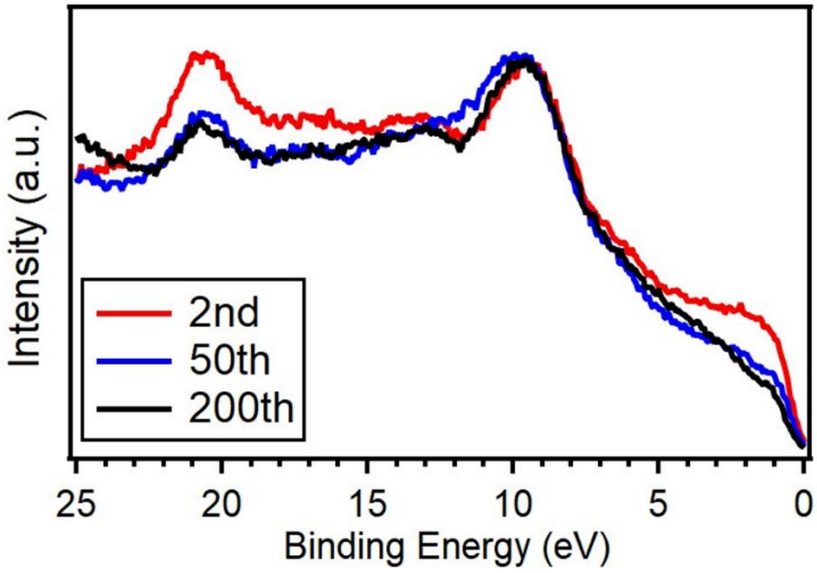

Figure 4.8. Valence band structure of charged Li-rich cathode under different cycles

For further distinguishing which elements attribute to the electron transfer from the Fermi level to the deeper energy level, the RXPS measurements are performed. Because different element has totally different excitation energy according to XAS results, the RXPS shows element sensitivity at valence band characterization. **Figure 4.9** to **Figure 4.11** show the RXPS results of Ni, Co and Mn respectively with the chosen excitation energy from XAS TEY mode results.

For Ni RXPS results, the 2nd cycled sample, at 1.5 eV and 3 eV, there is a shoulder and a small peak. These two peaks may be related to e_g* and t_{2g} orbital of Ni^{2+} or Ni^{3+} respectively but for RXPS there is less reference, so it needs further experiment for confirmation. Usually, the oxidation of TM and hybridization increase will cause a decrease in intensity near the Fermi level. However, considering Ni has a reduction under long-duration, this phenomenon cannot be explained by the oxidation of Ni. It is more reasonable that lattice structure change (layered to spinel) will increase the hybridization between Ni and O and cause the intensity to decrease.

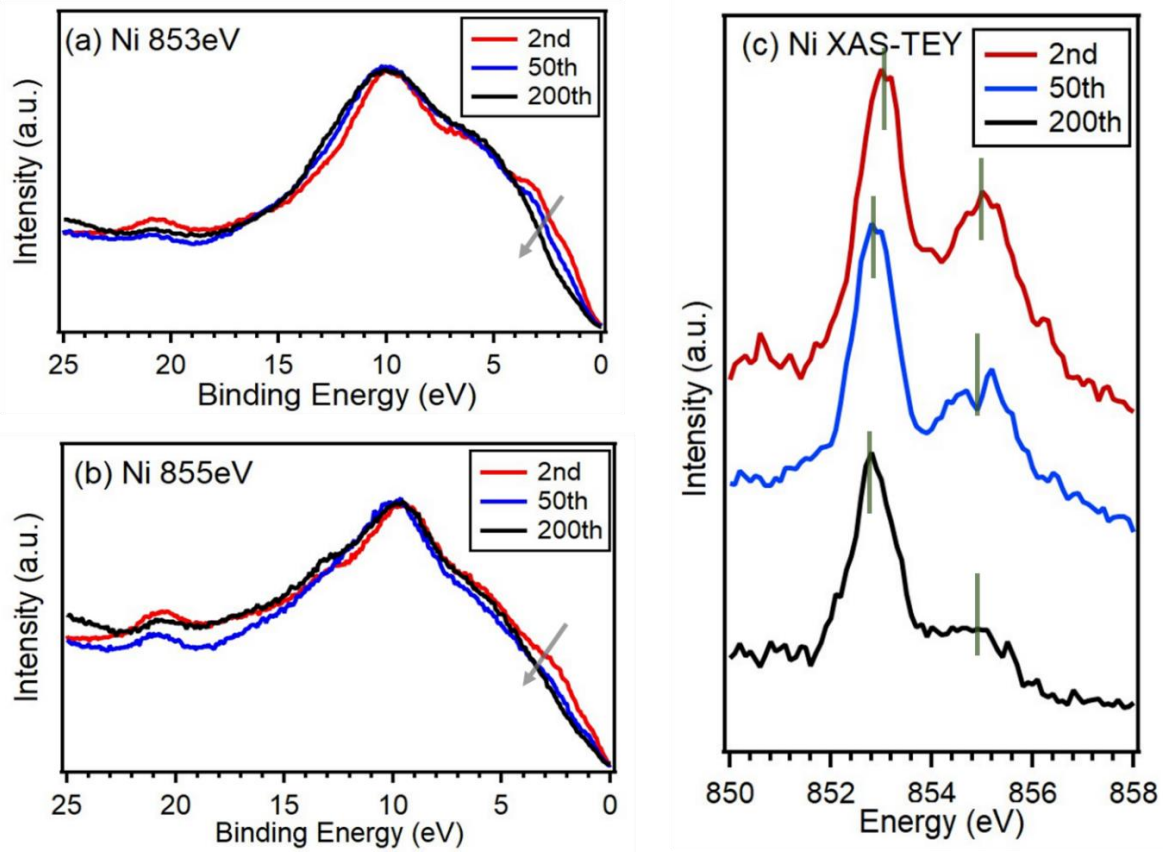

Figure 4.9. RXPS results with excitation energy of (a) at 853 eV and (b) 855 eV from (c) XAS-TEY results on Ni L_3-edges.

Such similar intensity decrease is also shown in Co RXPS results which can be explained by the hybridization increase due to the lattice structure change. It is worth noticing that both layered and spinel phase has octahedral coordination. Hence, the hybridization change is mainly because of the lattice parameter and bond length variation between layered and spinel phases.

For Mn RXPS results, because the first Mn^{4+} peak with excitation energy of 641 eV and Mn^{3+} peak with excitation energy of 641.9 eV is at the shoulder of Mn^{2+} peak with excitation energy of 640.5 eV. As a result, the RXPS of the first Mn^{4+} peak and Mn^{3+} peak are mixed with Mn^{2+} signal. Considering Mn^{2+} RXPS results have obvious characteristics that can be used to distinguish[84], here I only show the RXPS results with excitation energy of 640.5 eV (Mn^{2+}) and 643.5 eV (Mn^{4+} second peak). As shown in **Figure 4.11**, Mn^{4+} RXPS results show the same variation with Co and Ni which refer to the hybridization change due to spinel phase transition at the surface area. Whereas the Mn^{2+} RXPS results show a different variation. At the 50^{th} cycles, binding energy with 4 eV, the relative peak intensity shows an obvious increase which is related to the hybridization weakening. Such phenomenon is related to Mn^{2+} dissolving in electrolyte and CEI forming divalent manganese salt. Hence, the hybridization changes for Mn^{2+} are not only between Mn and O but also between Mn and organic compounds. The variation in Mn^{2+} RXPS results corroborates the evolution in CEI under long-duration.

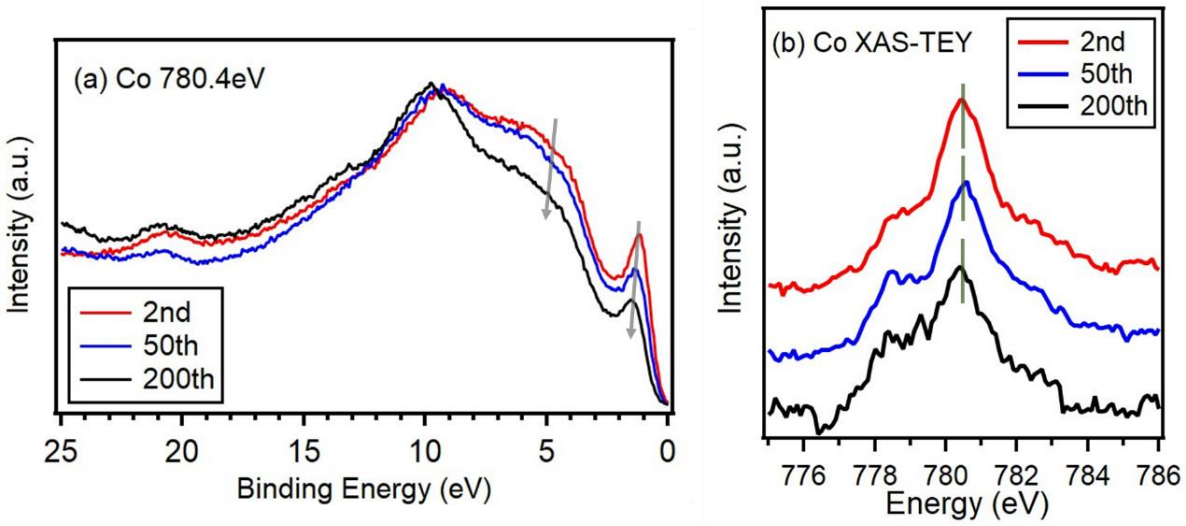

Figure 4.10. (a) RXPS result with excitation energy of 780.4 eV from (b) XAS-TEY results on Co L_3-edges.

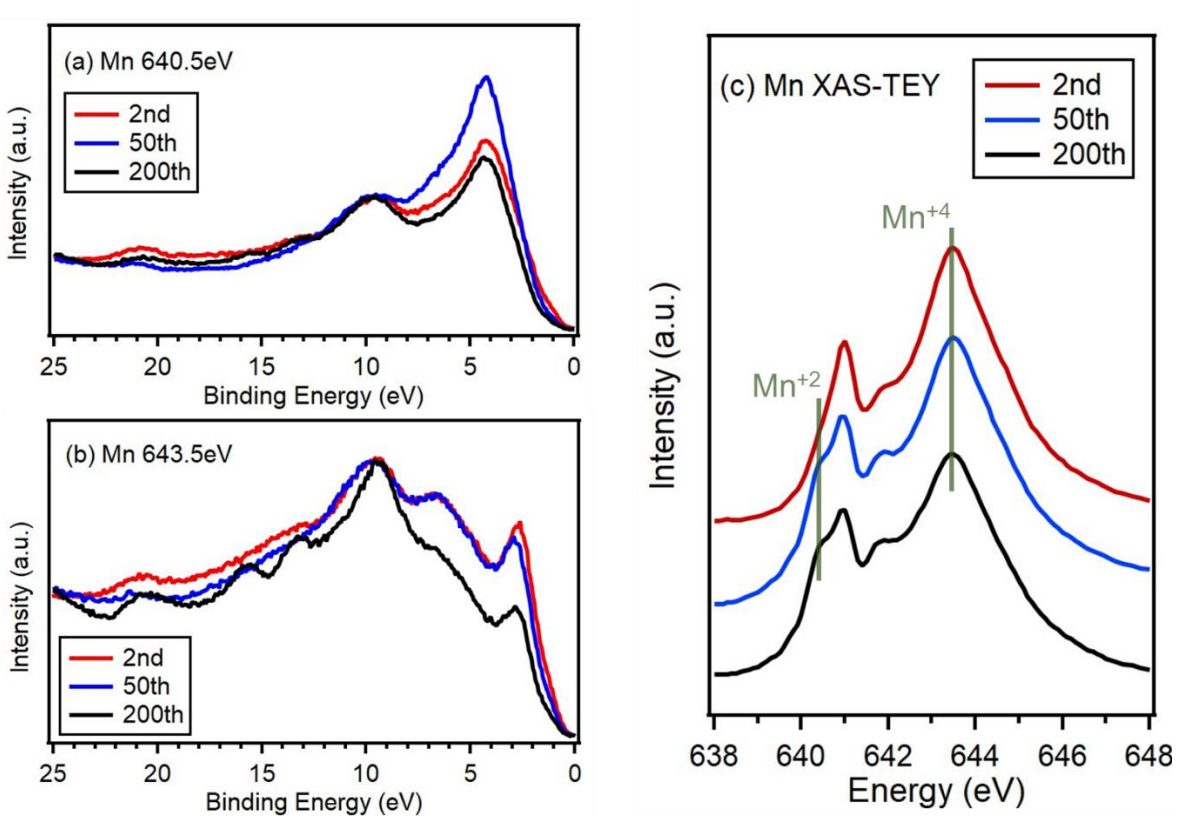

Figure 4.11. RXPS result with excitation energy of (a) 640.5 eV and (b) 643.5 eV from (c) XAS-TEY results on Mn L_3-edges.

As discussed previously, most TM ions have stronger hybridization with O due to the spinel phase transition. This hybridization change can also be revealed in O RXPS results. As shown in **Figure 4.12**, from 2 eV to 5 eV, the intensity shows an increase under long-duration. This indicates that the charge transfer from O to TM is enhanced and it is consistent with the previous results.

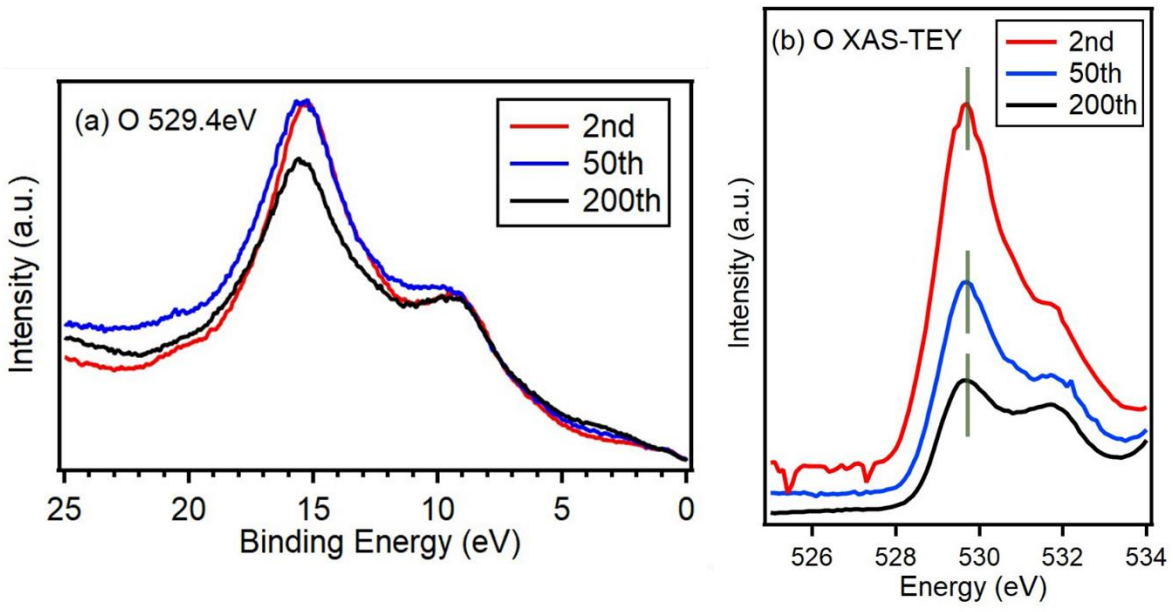

Figure 4.12. RXPS results with excitation energy of (a) 529.4 eV from (b) XAS-TEY results on O *K*-pre-edges.

4.2.3 Discussion and summary on XPS and RXPS results

The XPS results show the CEI evolution during cycling. First the thickness gets thicker under long-duration from the intensity of the TM-O peak. Second is the composition change under long-duration. In DSC measurement, if the cathode sample is mixed with an organic liquid electrolyte, the thermal stability will have an obvious decrease[16,96,97]. Although the detailed reaction is very complicated, it is no doubt that the existence of liquid electrolyte will do harm to thermal stability. Considering the CEI is also organic compounds formed from liquid electrolyte, composition and amount of CEI may influence thermal behavior, especially the onset temperature variation under long-duration.

The RXPS results show that the hybridization changes between TM and O under long-duration. This hybridization change is due to the lattice structure change from layered to spinel phase at the surface area. This spinel phase will inhibit the degradation rate and increase thermal safety kinetically.

Chapter 5 Summary

5.1 Summary

In this research, I focused on utilizing the electronic structure characterization to explain the mechanism of thermal behavior of Li-rich cathode materials under long-duration.

In chapter 3, from the typical electrochemical property the samples were qualified as normal Li-rich materials. More importantly, the DSC measurement showed the fine evolution of thermal behavior under long-duration, the phase transition rate change and onset temperature change. The reproducibility of the results has also been demonstrated through multiple experiments.

In chapter 4, the XAS, XPS and RXPS measurements were performed. From XAS results, the valence state of TM showed huge reduction at the surface area and tiny reduction at the bulk area because of the O_2 release. Due to the obvious phase transition at the surface area, the lattice structure evolution on the surface area can also be detected by XAS measurements with the TEY mode. From XPS and RXPS results, the electronic structure evolution of the core level and the valence band were revealed. Such evolution on the electronic structure indicates the growth of the CEI layer and the surface lattice-structure change.

In conclusion, the surface structure change from layered to spinel can explain the drop of the phase transition rate. For the onset temperature, it is more complicated and it may involve multiple factors. The reduction of TM in the bulk area will increase the onset temperature but the O defects in the layered structure and the growth of the CEI layer may do harm to it. The schematic is shown in **Figure 5.1**

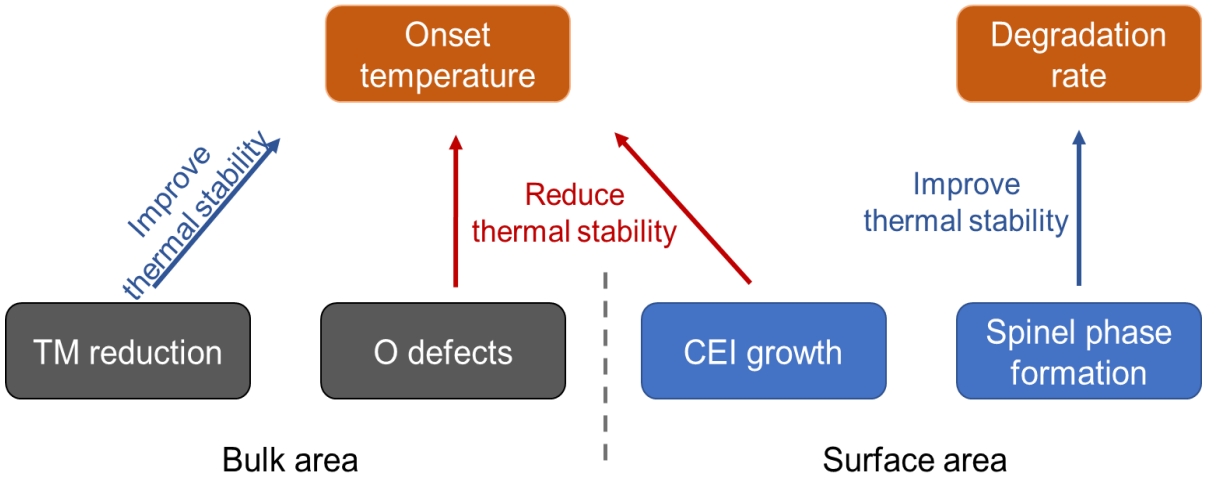

Figure 5.1 Schematic of research conclusion.

This research explains the reasons for thermal behavior changes from the perspective of electronic structure evolution and at bulk and surface area. Based on the above results, some methods to improve thermal stability are proposed, including coating a stable spinel film on the surface of cathode particles, and controlling the growth of CEI by electrolyte additives.

5.2 . Future Plan

There are some detailed problems needed to be resolved. First, the DSC results at the 200th cycles show 2 peak shapes that may be attributed to TM migration. Second, the influence of the high valence-state oxygen needs to be considered and high resolution RIXS is necessary for its characterization.

Also, in Li-rich cathode materials and other layered materials, the oxygen redox mechanism still has many problems to be resolved. Both normal layered cathode materials and Li-rich cathode materials show similar high valence-state oxygen fingerprints. However, up to now, no one can explain why different structure shows the same characteristic and I will keep researching this area.

For me personally, I plan to learn more data analysis and theoretical calculation methods so that I can explain the RXPS and RIXS result more precisely.

Reference

[1] M. S. Whittingham, Chemical Reviews **104**, 4271−4301 (2004).

[2] M. Winter, B. Barnett, and K. Xu, Chem Rev **118**, 11433 (2018).

[3] R. Chen, Q. Li, X. Yu, L. Chen, and H. Li, Chem Rev **120**, 6820 (2020).

[4] M. Armand and J. M. Tarascon, Nature **451**, 652 (2008).

[5] P. Roy and S. K. Srivastava, Journal of Materials Chemistry A **3**, 2454 (2015).

[6] G. Girishkumar, B. McCloskey, A. C. Luntz, S. Swanson, and W. Wilcke, The Journal of Physical Chemistry Letters **1**, 2193 (2010).

[7] E. Hu *et al.*, Nature Energy **3**, 690 (2018).

[8] Y. Li, X. Chen, A. Dolocan, Z. Cui, S. Xin, L. Xue, H. Xu, K. Park, and J. B. Goodenough, J Am Chem Soc **140**, 6448 (2018).

[9] F. Han, Y. Zhu, X. He, Y. Mo, and C. Wang, Advanced Energy Materials **6** (2016).

[10] J. Hong, H.-D. Lim, M. Lee, S.-W. Kim, H. Kim, S.-T. Oh, G.-C. Chung, and K. Kang, Chemistry of Materials **24**, 2692 (2012).

[11] H. U. Escobar-Hernandez, R. M. Gustafson, M. I. Papadaki, S. Sachdeva, and M. S. Mannan, Journal of The Electrochemical Society **163**, A2691 (2016).

[12] Z. Y. Jiang, H. B. Li, Z. G. Qu, and J. F. Zhang, International Journal of Hydrogen Energy **47**, 9428 (2022).

[13] J. Cho, Electrochemical and Solid-State Letters **2** (1999).

[14] H. Konishi, T. Yuasa, and M. Yoshikawa, Journal of Power Sources **196**, 6884 (2011).

[15] J. Geder, J. H. Song, S. H. Kang, and D. Y. W. Yu, Solid State Ionics **268**, 242 (2014).

[16] S. Muhammad, S. Lee, H. Kim, J. Yoon, D. Jang, J. Yoon, J.-H. Park, and W.-S. Yoon, Journal of Power Sources **285**, 156 (2015).

[17] L. Ji, Z. Lin, M. Alcoutlabi, and X. Zhang, Energy & Environmental Science **4** (2011).

[18] A. Yoshino, Angew Chem Int Ed Engl **51**, 5798 (2012).

[19] T. O. Raimu Endo, Kazunori Takada, Takuya Masuda, The Journal of Physical Chemistry Letters (2020).

[20] C. Zhao, T. Wada, V. De Andrade, D. Gürsoy, H. Kato, and Y.-c. K. Chen-Wiegart, Nano Energy **52**, 381 (2018).

[21] X. B. Cheng, R. Zhang, C. Z. Zhao, and Q. Zhang, Chem Rev **117**, 10403 (2017).

[22] M. Golozar, P. Hovington, A. Paolella, S. Bessette, M. Lagacé, P. Bouchard, H. Demers, R. Gauvin, and K. Zaghib, Nano Letters **18**, 7583 (2018).

[23] K. Xu, Chem Rev **114**, 11503 (2014).

[24] D. Rettenwander, R. Wagner, A. Reyer, M. Bonta, L. Cheng, M. M. Doeff, A. Limbeck, M. Wilkening, and G. Amthauer, J Phys Chem C Nanomater Interfaces **122**, 3780 (2018).

[25] X. W. Abhik Banerjee, Chengcheng Fang, Erik A. Wu, and Ying Shirley Meng, Chemical Reviews (2020).

[26] Q. Zhang, D. Cao, Y. Ma, A. Natan, P. Aurora, and H. Zhu, Advanced Materials **31** (2019).

[27] S. Smetaczek *et al.*, J Mater Chem A Mater **9**, 15226 (2021).

[28] A. A. Delluva, J. Dudoff, G. Teeter, and A. Holewinski, ACS Appl Mater Interfaces **12**, 24992 (2020).

[29] B. Gao, R. Jalem, and Y. Tateyama, ACS Applied Materials & Interfaces **12**, 16350 (2020).

[30] T. Thompson *et al.*, ACS Energy Letters **2**, 462 (2017).

[31] Y. Li, Z. Wang, Y. Cao, F. Du, C. Chen, Z. Cui, and X. Guo, Electrochimica Acta **180**, 37 (2015).

[32] Y. Zhu, X. He, and Y. Mo, ACS Appl Mater Interfaces **7**, 23685 (2015).

[33] M. M. Thackeray, W. I. F. David, P. G. Bruce, and J. B. Goodenough, Materials Research Bulletin **18**, 461 (1983).

[34] T. Ohzuku, M. Kitagawa, and T. Hirai, Journal of The Electrochemical Society **137**, 769 (1990).

[35] J. M. Tarascon and D. Guyomard, Electrochimica Acta **38**, 1221 (1993).

[36] G. Ceder, A. V. d. Ven, C. Marianetti, and D. Morgan, Modelling and Simulation in Materials Science and Engineering **8**, 311 (2000).

[37] Z. Deng, Y. Mo, and S. P. Ong, NPG Asia Materials **8**, e254 (2016).

[38] A. K. Padhi, K. S. Nanjundaswamy, and J. B. Goodenough, Journal of The Electrochemical Society **144**, 1188 (1997).

[39] Y. Huang *et al.*, Inorg Chem **55**, 4335 (2016).

[40] K.Mizushima, P.C.Jones, P.J.Wiseman, and J.B.Goodenough., Materials Research Bulletin **15**, 783 (1980).

[41] E. Hu *et al.*, Joule **5**, 720 (2021).

[42] J.-N. Zhang *et al.*, Nature Energy **4**, 594 (2019).

[43] Z. Chen and J. R. Dahn, Electrochimica Acta **49**, 1079 (2004).

[44] T. Ohzuku and A. Ueda, Journal of The Electrochemical Society **141**, 2972 (1994).

[45] P. Kalyani, S. Chitra, T. Mohan, and S. Gopukumar, Journal of Power Sources **80**, 103 (1999).

[46] M. H. Rossouw and M. M. Thackeray, Materials Research Bulletin **26**, 463 (1991).

[47] M. Zhang *et al.*, Nature Reviews Materials (2022).

[48] K. Numata, C. Sakaki, and S. Yamanaka, Chemistry Letters **26**, 725 (1997).

[49] K. Numata, C. Sakaki, and S. Yamanaka, Solid State Ionics **117**, 257 (1999).

[50] A. Boulineau, L. Simonin, J. F. Colin, C. Bourbon, and S. Patoux, Nano Lett **13**, 3857 (2013).

[51] W. Hua *et al.*, Nat Commun **10**, 5365 (2019).

[52] M. Sathiya *et al.*, Nat Mater **14**, 230 (2015).

[53] C. Genevois, H. Koga, L. Croguennec, M. Ménétrier, C. Delmas, and F. Weill, The Journal of Physical Chemistry C **119**, 75 (2014).

[54] Z. Wei, Y. Xia, B. Qiu, Q. Zhang, S. Han, and Z. Liu, Journal of Power Sources **281**, 7 (2015).

[55] B. Çetin, Z. Camtakan, and N. Yuca, Materials Letters **273** (2020).

[56] V. R. Galakhov, E. Z. Kurmaev, S. Uhlenbrock, M. Neumann, D. G. Kellerman, and V. S. Gorshkov, Solid State Communications **99**, 221 (1996).

[57] W.-S. Yoon, K.-B. Kim, M.-G. Kim, M.-K. Lee, H.-J. Shin, J.-M. Lee, J.-S. Lee, and C.-H. Yo, The Journal of Physical Chemistry B **106**, 2526 (2002).

[58] D. H. Seo, J. Lee, A. Urban, R. Malik, S. Kang, and G. Ceder, Nat Chem **8**, 692 (2016).

[59] M. Okubo and A. Yamada, ACS Appl Mater Interfaces **9**, 36463 (2017).

[60] T. Sudayama *et al.*, Energy & Environmental Science **13**, 1492 (2020).

[61] D. A. Kitchaev, J. Vinckeviciute, and A. Van der Ven, J Am Chem Soc **143**, 1908 (2021).

[62] R. A. House *et al.*, Nature Energy **5**, 777 (2020).

[63] R. A. House *et al.*, Nature **577**, 502 (2020).

[64] R. A. House, J. J. Marie, J. Park, G. J. Rees, S. Agrestini, A. Nag, M. Garcia-Fernandez, K. J. Zhou, and P. G. Bruce, Nat Commun **12**, 2975 (2021).

[65] R. A. House, J.-J. Marie, M. A. Pérez-Osorio, G. J. Rees, E. Boivin, and P. G. Bruce, Nature Energy **6**, 781 (2021).

[66] C. H. Shen, L. Huang, Z. Lin, S. Y. Shen, Q. Wang, H. Su, F. Fu, and X. M. Zheng, ACS Appl Mater Interfaces **6**, 13271 (2014).

[67] W. E. Gent *et al.*, Nat Commun **8**, 2091 (2017).

[68] D. Eum *et al.*, Nat Mater **19**, 419 (2020).

[69] E. McCalla *et al.*, Science **350**, 1516 (2015).

[70] D. Eum *et al.*, Nat Mater (2022).

[71] E. Zhao *et al.*, Energy Storage Materials **16**, 354 (2019).

[72] Q. Li *et al.*, Journal of Physics D: Applied Physics **49** (2016).

[73] M. Oishi *et al.*, Journal of Materials Chemistry A **4**, 9293 (2016).

[74] W. Yang and T. P. Devereaux, Journal of Power Sources **389**, 188 (2018).

[75] F. Frati, M. Hunault, and F. M. F. de Groot, Chem Rev **120**, 4056 (2020).

[76] D. Asakura *et al.*, AIP Advances **6** (2016).

[77] D. Asakura, Y. Nanba, E. Hosono, M. Okubo, H. Niwa, H. Kiuchi, J. Miyawaki, and Y. Harada, Physical Chemistry Chemical Physics **21**, 18363 (2019).

[78] Z. Zhuo *et al.*, Joule **5**, 975 (2021).

[79] X. Liu *et al.*, Nature Energy (2022).

[80] Z. Zhuo *et al.*, J Phys Chem Lett **9**, 6378 (2018).

[81] W. Zuo *et al.*, Energy & Environmental Science **13**, 4450 (2020).

[82] in *NETZSCH DSC Instructions*.

[83] U. Fano, Physical Review **124**, 1866 (1961).

[84] S. Kurosumi, The University of Tokyo, 2011.

[85] X. Liu, D. Wang, G. Liu, V. Srinivasan, Z. Liu, Z. Hussain, and W. Yang, Nat Commun **4**, 2568 (2013).

[86] N. Zhang *et al.*, ACS Applied Energy Materials **1**, 5968 (2018).

[87] J. Xu *et al.*, Nat Commun **9**, 947 (2018).

[88] J. Rana *et al.*, ACS Energy Letters **5**, 634 (2020).

[89] J. Xiong, Z. Liang, Q. Guo, M. Zhou, H. Potapenko, and S. Zhong, Energy & Fuels **35**, 15143 (2021).

[90] H. Sun *et al.*, Advanced Functional Materials **32** (2022).

[91] S. L. Spence, Z. Xu, S. Sainio, D. Nordlund, and F. Lin, Inorg Chem **59**, 10591 (2020).

[92] K. Ariyoshi, H. Yamamoto, and Y. Yamada, Electrochimica Acta **260**, 498 (2018).

[93] T. Mizokawa *et al.*, Phys Rev Lett **111**, 056404 (2013).

[94] V. R. Galakhov *et al.*, Physical Review B **74** (2006).

[95] Y. Furushima, C. Yanagisawa, T. Nakagawa, Y. Aoki, and N. Muraki, Journal of Power Sources **196**, 2260 (2011).

[96] H. F. Xiang, H. Wang, C. H. Chen, X. W. Ge, S. Guo, J. H. Sun, and W. Q. Hu, Journal of Power Sources **191**, 575 (2009).

[97] Y. Yu, J. Wang, P. Zhang, and J. Zhao, Journal of Energy Storage **12**, 37 (2017).

Acknowledgement

I’m eternally grateful for Professor Yoshihisa Harada for giving me many instructions on electronic structure. Also, during my time in China, I asked many questions in X-ray spectroscopy and Harada-sensei answered my questions very patiently. In addition, Harada-sensei also gave me many advise on presentation and life in Japan. Thank you from bottom of my heart.

Kiuchi-sensei, Zhang-san and Mustafa-san gave me many advice on Li-ion battery research. Kiuchi-sensei also had many discussions with me on cathode materials mechanism. Zhang-san provided great support for experimental setups. I am very thankful for your help. Liu-san give me some ideas and information on electrochemistry.

Kurahashi-san, Ralph-san and Tatsuta-san gave help on life in Japan and laboratory. Especially Ralph-san helped me to register many documents when I came to SPring-8. I appreciate very much.

I’d like to express my deepest gratitude to Professor Xiqian Yu at Institute of Physics Chinese Academy of Sciences for supporting my research during the period when I could not enter Japan due to the coronavirus pandemic. Also, Junyang Wang, Mingwei Zan, Xinyi Yang and other students had many discussions with me and helped me a lot. I am grateful for them.